

MAGNETOFLUID-DYNAMIC DRAG MEASUREMENTS ON
SEMI-INFINITE BODIES IN ALIGNED FIELDS

Thesis by
Bob Hiro Suzuki

In Partial Fulfillment of the Requirements
For the Degree of
Doctor of Philosophy

California Institute of Technology
Pasadena, California

1967

(Submitted May 4, 1967)

ACKNOWLEDGMENT

First and foremost, I wish to express my sincere gratitude to Dr. Hans W. Liepmann for his steady encouragement and guidance throughout the course of this research.

I am also indebted to Mr. Bruce M. Lake for his assistance with the experiments and to the GALCIT staff for their help. Further thanks are due Mrs. Linda L. Palmrose for the typing of the manuscript.

I gratefully acknowledge the National Aeronautics and Space Administration and the Ford Foundation for their financial assistance and the Office of Naval Research for their support of the research program under contract N-onr-220(21).

Finally, I must express my heartfelt thanks to my wife, Agnes, for her encouragement and fortitude without which this work could never have been completed.

ABSTRACT

Experiments are described in which measurements were made of the drag of semi-infinite bodies moving parallel to a uniform magnetic field in a conducting fluid. Two of these bodies were moderately streamlined halfbodies and a third was a blunt halfbody. The drag coefficients of all three bodies were found to increase monotonically as a function of the interaction parameter, N . This parameter was varied in the experiments from 0 to about 24. The drag coefficients of the streamlined halfbodies were found to increase linearly with N for $N \leq 0(1)$ in agreement with a simple theory based on a calculation of the Joule dissipation. On the other hand, for the same range of N , the drag coefficient of the blunt halfbody was found to increase negligibly from its zero-field value of 0.66. For $N \gg 1$, the drag coefficients of all three bodies were of $O(1)$ and appeared to be asymptotically converging to some common limiting value. Although the drag could not be calculated for large, finite values of N , an inviscid theoretical model of the flow is described from which it is concluded that the drag coefficient of any halfbody must approach unity as $N \rightarrow \infty$.

In addition to the experiments with the semi-infinite bodies, experiments are also described in which measurements were made of the non-magnetic drag of impulsively-started flat disks. Some unexpected and interesting transient variations in this drag were observed and are attributed to the vortex formation process in the wake.

TABLE OF CONTENTS

CHAPTER	TITLE	PAGE
	Acknowledgment	ii
	Abstract	iii
	List of Figures	vi
	List of Symbols	viii
I.	INTRODUCTION	1
II.	DESCRIPTION OF EXPERIMENTS	9
	2.1 The Mercury Tow Tank	9
	2.2 The Drag Balance	10
	2.3 The Drag Models	13
	2.4 Experimental Procedure	17
	2.5 Data Reduction Procedure	19
III.	RESULTS OF EXPERIMENTS	28
	3.1 MFD Drag of Semi-Infinite Bodies	28
	3.2 Drag of Impulsively-Started Flat Disks	31
	3.3 Discussion of Uncertainties	37
IV.	THEORETICAL DISCUSSION	40
	4.1 Weak Interaction Case, $N \ll 1$	40
	4.2 Strong Interaction Case, $N \gg 1$	58
V.	CONCLUSION	69
	REFERENCES	71
	APPENDICES	76
	A. Calculation of Base Drag without Dissipation	76

CHAPTER	TITLE	PAGE
B.	Calculation of Pressure Jump due to Flow in Standpipe	77
C.	Calculation of Base Drag with Dissipation	79
D.	Derivation of MFD Boundary Layer Equations	83
FIGURES		87

LIST OF FIGURES

1. Currents and Magnetic Forces in Axisymmetric MFD Flow in the Limit $R_m \rightarrow 0$
2. Schematic Diagram of the Mercury Tow Tank
3. Design of Drag Balance
4. Diagram of the Drag Balance Electrical Circuit
5. Drag Balance Set-Ups for Flat Disk
6. Head Forms of Semi-Infinite Bodies
7. Typical Drag Balance Calibration Curves
8. Drag Data of Rankine Halfbody at Various Field Strengths and at a Fixed Velocity of 0.3 m/sec
9. Transient Drag Data of Flat Disks at Fixed Velocity of 0.3 m/sec
10. Control Volume for Calculation of Base Drag
11. Zero-Field Drag Coefficients of Semi-Infinite Bodies vs. Reynolds Number
12. Drag Coefficients of Semi-Infinite Bodies vs. Interaction Parameter
13. MFD Drag Coefficient of Rankine Halfbody vs. Reynolds Number at Various Hartmann Numbers
14. Drag of Flat Disks Started Impulsively from Rest to a Constant Velocity of 0.3 m/sec
15. Drag Coefficients of 0.75 in. Diameter Flat Disk Started Impulsively from Rest
16. MFD Drag Coefficient of Rankine Halfbody vs. Interaction Parameter

17. Tamada's Solution (Ref. 32) for Inviscid MFD Flow Past a Two-Dimensional Circular Cylinder at $N = .4$
18. Control Volumes for Calculation of MFD Drag
19. Solution for the Limit $N \rightarrow \infty$
20. Development of Current Layers for $N \gg 1$
21. Ultimate Flow Field in the Limit as $N \rightarrow \infty$

LIST OF SYMBOLS

$\underline{B} = \underline{B}^*/B_o$	dimensionless magnetic field
B_o	uniform applied magnetic field
d	diameter of halfbody
$F = 1 - u(x \rightarrow + \infty)$	downstream vortical wake function
$\underline{j} = \underline{j}^*/\sigma UB_o$	dimensionless current density
$p = p^* - p_1/\rho U^2$	dimensionless pressure
p_1	static pressure at upstream infinity
p_b	pressure at base of halfbody model
$\underline{q} = \underline{q}^*/U$	dimensionless velocity
r, x	cylindrical coordinates transverse and parallel to freestream direction, respectively
$u_1 = U$	velocity at upstream infinity
u_2	velocity at downstream infinity, or velocity of drive shaft
$u = u^*/U$	dimensionless x-component of velocity
$v = v^*/U$	dimensionless radial or y-component of velocity
δ	current or boundary layer thickness
ρ	density
σ	electrical conductivity
ν	kinematic viscosity
μ	permeability
Δ	Kármán-Pohlhausen parameter (see appendix D)

Dimensionless Parameters:

$\alpha = B_o/U \sqrt{\rho\mu}$	Alfvén number
---------------------------------	---------------

$$C_D = D / \frac{1}{2} \rho U^2 \frac{\pi}{4} d^2$$

drag coefficient

$$C_{D_b} = (p_b - p_1) / \frac{1}{2} \rho U^2$$

base drag coefficient

$$C_{D_v} = D_v / \frac{1}{2} \rho U^2 \frac{\pi}{4} d^2$$

viscous drag coefficient

$$Ha = B_o d \sqrt{\sigma / \rho \nu}$$

Hartmann number

$$N = \sigma B_o^2 d / \rho U$$

interaction parameter

$$Re = Ud / \nu$$

Reynolds number

$$Rm = \mu \sigma U d$$

magnetic Reynolds number

I. INTRODUCTION

Experimental research in incompressible magnetofluid-dynamics (MFD) was initiated at GALCIT in 1960 with the construction of a mercury tow tank facility designed for the study of MFD flows past bodies (see reference 1). At that time, not a single experiment on such flows was known to have been performed; whereas the theory had been worked out for a number of different cases under a wide variety of assumptions (see e. g. , references 2 through 6). The need for experiments to test the various theoretical solutions that had been proposed was rather apparent; but it was perhaps even more compelling to conduct experiments to study fundamentally important regimes of flow which so far had not been amenable to theoretical analysis (e. g. , transition at high Reynolds number).

Since 1960, various investigators have carried out experiments which have to some extent met these demands. Maxworthy (Ref. 7) has measured the drag of freely-descending spheres dropped into liquid sodium; Ahlstrom (Ref. 8), in an experiment in the GALCIT facility, has measured the magnetic field perturbations produced ahead of a semi-infinite Rankine body; Motz (Ref. 9) has determined the drag and induced electric field of an oscillating sphere in mercury; and most recently, Yonas (Ref. 10) has measured the drag of spheres and of a flat disk in a liquid sodium tunnel. In all of these experiments the applied magnetic field was aligned parallel to either the uniform flow or to the motion of the body. The only other experiment on MFD flows past bodies appears to be that of Dorman and Mikhailov (Ref. 11) who measured the induced magnetic and electric fields of a sphere

moving perpendicular to an applied magnetic field in mercury. That more experiments have not been performed attests to the difficulties involved in setting up such experiments. A problem almost inherent in MFD experiments is the rather long-range effects which the boundaries can have on the flow via the Alfvén wave mechanism. Such boundary effects appear to have been encountered, to a greater or lesser degree, in all of the experiments described. The results of some of these experiments -- in particular, those relevant to the present work -- will be described in later sections.

The experiments considered here were the latest to be performed in the GALCIT mercury tow tank and were mainly concerned with the drag of semi-infinite bodies moving parallel to an applied magnetic field. The drag was measured with a force transducer which was specially designed and developed for use in the tow tank. The description of the experiments will be covered in chapter II and their results presented in chapter III. However, before proceeding to these discussions, some preliminary discussion is in order on the general theoretical problem of MFD flows past bodies in aligned magnetic fields.

The equations, in dimensionless form, governing the steady laminar flow of an incompressible, viscous and electrically conducting fluid are (Ref. 12)

$$\nabla \cdot \mathbf{q} = 0 \quad (1.1a)$$

$$(\mathbf{q} \cdot \nabla) \mathbf{q} = -\nabla p + N(\mathbf{j} \times \mathbf{B}) + \frac{1}{Re} \nabla^2 \mathbf{q} \quad (1.1b)$$

$$(\underline{q} \cdot \nabla) \underline{B} - (\underline{B} \cdot \nabla) \underline{q} = \frac{1}{Rm} \nabla^2 \underline{B} \quad (1.1c)$$

where¹:

$$\underline{x} = \frac{\underline{x}^*}{d}, \quad \underline{q} = \frac{\underline{q}^*}{U}, \quad \underline{B} = \frac{\underline{B}^*}{B_0}, \quad \underline{j} = \frac{\underline{j}^*}{\sigma U B_0}, \quad p = \frac{p^* - p_1}{\rho U^2}$$

The starred quantities denote dimensional quantities, and we shall follow this designation henceforth. The three dimensionless parameters appearing in these equations are the Reynolds number Re , the magnetic Reynolds number Rm and the interaction parameter N , which are defined by

$$Re = \frac{Ud}{\nu} \sim [\text{inertia force/viscous force}]$$

$$Rm = \mu \sigma U d \sim [\text{body speed/magnetic diffusion speed}]^2$$

$$N = \frac{\sigma B_0^2 d}{\rho U} \sim [\text{magnetic force/inertia force}]$$

These three parameters together with the force coefficient can be shown to completely characterize the problem (Ref. 1) and are the most convenient ones for our purposes here. Two other commonly-used dimensionless parameters, which may be expressed in terms of those chosen above, are the Hartmann number:

¹ The definitions of the various symbols may be found in the List of Symbols on p.viii.

$$Ha = \sqrt{N Re} = B_o d \sqrt{\frac{\sigma}{\rho \nu}} \sim [\text{magnetic force/viscous force}]^{\frac{1}{2}}$$

and the Alfvén number:

$$\alpha = \sqrt{\frac{N}{Rm}} = \frac{B_o}{U \sqrt{\rho \mu}} \sim [\text{Alfvén speed/body speed}]$$

At this point, we may gain some perspective on the practical aspects of the problem by considering what the ranges of these parameters are in laboratory experiments. In the present experiments and in those cited earlier, the achievable conditions were limited to

$$2 \times 10^3 < Re < 5 \times 10^5, \quad 0 \leq N < 100$$

$$Rm \left\{ \begin{array}{ll} \ll 1 & \text{in Hg} \\ \leq 0(1) & \text{in Na} \end{array} \right.$$

And in general, it is probably quite realistic to set the limits, $Re \gg 1$ and $N \ll Re$, on the conditions which can presently be achieved in laboratory experiments, at least with the common terrestrial liquid metals.

The practical limits established above have important implications when they are compared with the conditions assumed in the various existing theoretical solutions on MFD flows past bodies. Such a comparison has been made by Yonas (Ref. 10) who comes to the conclusion that most of these solutions are for problems which

cannot be physically realized². For example, he shows that the conditions appropriate to $Rm = \infty$ are far from being approached in the laboratory, and concludes that the well-known controversy over the solution for this case of Sears and Resler (Ref. 4) on the one hand, and that of Stewartson (Ref. 5) on the other, is quite unlikely to be resolved through experiments. He also points out that even the modified Stokes problem treated by Chester (Ref. 13), which seems quite physically realistic, would be extremely difficult to verify experimentally since the condition, $Ha \gg Re$, is required. The limitations of these and many other theories were discussed at some length by Yonas, and we hardly need to go through such a discussion again here. The only point we note is that despite all the existing theories, he was unable to find a single one which could describe the results of his experiments. In order to explain these results, he proposed a nonlinear theoretical model of his flow (c. f., Sec. 4.2), but left some subtle, basic questions unanswered.

In the case of the present experiments, because of simpler flow conditions, the theory is considerably better defined. For the case $N \ll 1$, the drag of streamlined semi-infinite bodies can be calculated explicitly. And in the general case of arbitrary N , it will be seen that a fairly complete picture of the flow is obtainable through a strictly inviscid theoretical model. We defer detailed discussion of the theory until chapter IV. However, it will be

² Some of these solutions could conceivably find application in astrophysical phenomena, but he is presumably excluding such exotic possibilities.

convenient for us to reduce eqns. (1.1) now to the considerably simpler form in which they are used in chapter IV. This will be done by invoking a pair of assumptions which are consistent with the conditions of the experiments.

The first assumption is that the magnetic field is everywhere equal to the uniform applied field; i. e., $\underline{B}^* = -B_0 \underline{i}$ (see figure 1). This assumption is consistent with the condition, $Rm \ll 1$, and can be inferred from Ampere's law:

$$\nabla \times \underline{B} = Rm \underline{j} = Rm (\underline{q} \times \underline{B})$$

The last equality follows from Ohm's law since $\underline{E} = 0$ in axisymmetric flows. This equation suggests that the change in field is³

$$\Delta \underline{B} = 0(Rm)$$

for $\underline{B}, \underline{q} = 0(1)$. In effect, what this says is that the fluid (Hg) is such a poor conductor that it may to a first approximation be treated as a nonconducting medium. Direct confirmation is provided by Ahlstrom's measurements (Ref. 8) which have shown that the induced fields are less than 1 per cent of the applied magnetic field strengths.

Thus, the assumption appears to be a very reasonable one and results in a considerable simplification because it effectively uncouples the momentum equation from the induction equation. Since the current density is now given by $\underline{j} = -\underline{q} \times \underline{i} = -v \underline{i}_\theta$, the magnetic force term in eqn. (1.1b) is reduced to

³ This is a conservative estimate because for $N \gg 1$ Childress (Ref. 34) shows that $\Delta \underline{B} = 0(Rm/N)$.

$$N (\underline{j} \times \underline{B}) = N (-v_{i_\theta} \times \underline{i}) = -N v_{i_r}$$

where v is the radial velocity component. A rather simple picture of the currents and magnetic forces can now be drawn as shown in figure 1. The currents flow in rings about the axis of the body and the current density at any radius is just proportional to the radial velocity at that radius. The magnetic force acts in a direction directly opposing the radial motion and is also just proportional to the radial velocity.

The second simplifying assumption is that the flow is inviscid; i. e., $Re = \infty$. Although this is consistent with the condition, $Re \gg 1$, it certainly would not be very meaningful if the flow is separated and/or turbulent. However, hindsight gained from the experiments indicates that the flows past the Rankine and ogive halfbodies may always be laminar and unseparated, and that the same may be true for the blunt halfbody at large values of N . In any case, we can invoke the assumption a posteriori. This assumption together with the former then reduces the momentum equation to the form:

$$(\underline{q} \cdot \nabla) \underline{q} = -\nabla p - N v_{i_r}$$

Note that the only parameter left in this equation is the interaction parameter, N . Therefore, if this is the correct equation for the flow, we should expect the drag coefficient to be a function of N alone; i. e., $C_D = f(N)$.

We must finally mention that in addition to the MFD drag measurements on the semi-infinite bodies, measurements were also made of the non-magnetic transient drag of a flat disk. Very interesting

effects in the behavior of this transient drag were somewhat inadvertently observed during unsuccessful attempts to measure the MFD drag of the disk. Since almost identical measurement techniques were involved, we found it convenient to describe these measurements concurrently with the others.

II. DESCRIPTION OF EXPERIMENTS

2.1 The Mercury Tow Tank

The GALCIT mercury tow tank facility consists essentially of a cylindrical stainless steel tank, $5\frac{1}{2}$ in. in internal diameter and 55 in. long, which is filled with about 700 lb. of mercury (see figure 2). Surrounding the tank is a water-cooled copper solenoid which can produce steady, axial magnetic fields up to 12 kilogauss in strength. Measurements with a Hall-effect probe have shown that the magnetic fields are uniform axially to 5 per cent and uniform radially to 2 per cent in the middle 25 in. of the solenoid.

Models are driven through the mercury on the end of a hollow 1 in. OD stainless steel shaft which passes through a graphitar sleeve bearing at the bottom of the tank. It is from this feature that the facility receives its designation as a tow tank. The shaft itself is driven through a system of cables and a magnetic clutch by a variable-speed electric motor capable of driving the shaft at speeds up to 3 m/sec.

The velocity of the drive shaft is measured by means of a velocity servo consisting of a rotating potentiometer geared to the cable drive. The voltage output of the potentiometer, which is directly proportional to the distance traveled by the drive shaft, is electronically differentiated to give a voltage output directly proportional to the drive shaft velocity. The drive shaft was found to accelerate to constant velocity in 2 to 3 inches and was usually allowed to travel a total distance of 30 to 36 inches.

The top of the tow tank is covered by a lucite transition section which leads into a 1 in. ID pyrex standpipe. When the drive shaft moves upward into the tank, it displaces mercury into the standpipe. Since the ID of the standpipe is the same as the OD of the drive shaft, the mercury level in the standpipe rises at the same rate as the shaft, thereby keeping the hydrostatic pressure acting on the end of the shaft constant. We shall explain in the next section why it was necessary to maintain this constant hydrostatic head.

Further details about the design and construction of the GALCIT mercury tow tank facility may be found in reference 1.

2.2 The Drag Balance

An earlier attempt (see Ref. 1) to measure drag in the tow tank consisted of timing the ascent of freely-rising spheres. However, the measurements did not yield an accurate check on the accepted standard values for sphere drag at zero magnetic field strength; and it was subsequently discovered that the spheres did not rise vertically along a straight path, but spiraled upward along a helical path. Consequently, this technique was abandoned and efforts were directed toward the development of a force transducer, or drag balance, which could be mounted on the end of the tow tank drive shaft. Several early versions of such a balance were tried, including capacitance and piezo-electric devices, but were unsuccessful due mainly to difficulties associated with rather peculiar pressure, acceleration and vibration forces which are produced in the tow tank.

The drag balance that was finally developed and successfully used in the present experiments is basically a simple damped spring-mass system in which the displacement of the spring produced by the drag force is converted into an output voltage. Two identical stainless steel bellows having a combined spring constant of around 40 lb/in serve as the spring. These are mounted with an epoxy cement, one 3 inches above the other, inside of a 1 in. OD stainless steel cylinder which simply becomes a continuation of the drive shaft (see figure 3). The end plates of the two bellows are connected by an 11/64 in. diameter shaft which has an extension above the upper bellows that serves as a sting for supporting models. Mounted near the mid-point of this shaft is a short length of 1/8 in. diameter fiber-optics image conduit¹ with a miniature lamp attached to one end. The light from the lamp is transmitted by the image conduit to its other end which is masked to collimate the emitted light into a thin beam. This light beam falls on a photoelectric transducer² which converts any displacements of the beam into changes in voltage. Damping for this spring-mass system was provided by filling the lower bellows and a small reservoir above it with a silicon oil having a viscosity of 800 centistokes. The interior of the balance was sealed from the mercury by the use of O-rings (not shown in figure 3).

¹ Product of the American Optical Co. Its purpose was to remove the lamp from the proximity of the photoelectric transducer in order to reduce voltage drift of the transducer due to heating.

² Trade name: Photopot, manufactured by the Giannini Controls Corp. This transducer is in essence a miniature ($\frac{1}{4} \times \frac{1}{4}$ in. square) slide-wire potentiometer in which the slide-wire is replaced by the frictionless light beam.

The necessary electrical leads for the balance were supplied by a 3-conductor shielded cable brought up through the hollow drive shaft. A diagram of the electrical circuit employed for the balance is given in figure 4. The photoelectric transducer was incorporated into a bridge circuit using a floating 9 V battery supply. The bridge output was passed through a low-pass filter which cut-off noise components above about 45 cps before being fed into the amplifier of a dual-beam oscilloscope. Current for the miniature lamp was provided by a 5 V regulated power supply. The overall frequency response of the system was just that of the low-pass filter since the balance had a frequency response of around 50 cps.

One other important feature of the drag balance that should be described is the incorporation of the static pressure holes which lead into the chamber surrounding the lower bellows. These holes allow the hydrostatic pressure of the mercury to act on the lower bellows so as to produce an upward force which can counterbalance the downward force produced by the hydrostatic pressure acting on the upper bellows. This counterbalancing scheme was essential for the successful operation of the balance because it rendered the balance insensitive to the pressure changes which were produced in the tow tank³. There was always a large initial pressure jump (which is calculated in appendix B) caused by the mercury accelerating into the standpipe. Moreover,

3

However, due to a slight difference (about 2%) in the surface areas of the bellows, the balance was not totally insensitive to changes in pressure. A very small correction due to this unbalance is given in Sec. 2.5.

this pressure jump was accompanied by low frequency (~ 6 cps), slowly-damped fluctuations in pressure caused by the oscillation of the mercury in the standpipe. A previous version of the present drag balance, designed by Dr. H. G. Ahlstrom, was unsuccessful because the hydrostatic pressure was allowed to act only on the upper bellows so that the pressure changes which occurred were not balanced out and completely obliterated the desired measurement.

At one time it was thought that the tow tank could be operated without the standpipe (i. e. , with a free surface of mercury at a fixed level) since the balance with its counterbalancing feature would be relatively unaffected even by the tremendous decrease (over 1 atmosphere) in hydrostatic pressure to which it would then be subjected. Unfortunately, it was found that tiny air bubbles trapped between the convolutions of the bellows would expand under the large negative pressure gradient and cause the balance to respond in a very erratic, unsatisfactory manner. Although various schemes were tried, such as placing the entire tow tank under vacuum, these air bubbles could never be eliminated to the point where they were not a problem. Consequently, we decided to retain the standpipe since it circumvented the problem by keeping the hydrostatic pressure on the balance constant.

2.3 The Drag Models

The first drag measurements with the balance were made on a flat disk. This model was selected for the initial measurements because its high drag was relatively easy to measure and could be

readily checked since its non-magnetic drag coefficient has a constant, stable value at high Reynolds numbers ($C_D = 1.17$ for $Re > 10^3$ according to Ref. 14). For these measurements, the top of the balance was capped by a lucite cone and the flat disk, also made of lucite, was mounted on the end of an 8 in. long, 1/8 in. diameter stainless steel sting which extended through a hole in the cone from the sting mount on the upper bellows (see figure 5a). However, this set-up subjected the balance not only to the drag force of the disk, but also to an unwanted force due to the dynamic pressure in the wake of the disk acting on the upper bellows. Therefore, a separate measurement of this "tare drag" force was necessary and was made by mounting the sting independently as shown in figure 5b such that the drag force of the disk was not transmitted to the balance. Three different size disks of diameters .50 in., .75 in. and 1.00 in. were used in these measurements.

As mentioned in the Introduction, the MFD drag measurements on the disk were not successful. The main difficulty was an uncertainty about the upstream influence of the drag balance on the flow in the wake of the disk. This did not appear to have an important effect on the non-magnetic drag (c. f., Sec. 3.2); but with the magnetic field present, the upstream propagation of Alfvén waves results in the formation of the so-called "upstream wake" (Ref. 8) ahead of the balance which may have interacted strongly with the downstream wake of the disk. Although this problem had been anticipated, we had hoped to resolve it experimentally by measuring the MFD drag with stings of different lengths and extrapolating the results. However, the results

of such measurements were inconclusive since no significant change in the drag was observed over a variation in sting length from 4 in. to 8 in. The MFD drag was always found to be slightly lower (10 per cent at most) than the non-magnetic drag even at the strongest field strength corresponding to an N of 20. These results are in complete disagreement with those obtained in the liquid sodium tunnel experiments of Yonas (Ref. 10; also see Sec. 3.1) who found that the drag of a disk increased about 75 per cent over the same range of N . The only major difference between the two experiments appears to be that in Yonas' experiments there was no body, such as a drag balance or strut, located downstream of the disk; the disk being suspended by wires from the tunnel walls. Therefore, the most plausible explanation at the present time for the discrepancy between the results of the experiments is that the MFD drag of the disk in the mercury tow tank experiments was unduly influenced by the presence of the drag balance. However, in chapter IV we shall mention an interesting inviscid theory for closed bodies which predicts that $C_D \rightarrow 1$ as $N \rightarrow \infty$, with stagnation pressure developing on the front of the body and freestream static pressure on the rear. This is the trend observed in our disk drag data, and one might speculate whether the presence of the drag balance may have produced conditions appropriate to this theory.

The difficulty encountered in the measurements on the disk undoubtedly would also have been encountered with any closed body since the drag balance would necessarily have to be located in the wake of such bodies. A semi-infinite body, however, avoids this difficulty by allowing the drag balance to become a part of the model

itself. Ideally, a semi-infinite body consists of a head form followed by an infinitely-long afterbody of circular cross-section. Such a body was easily simulated in the tow tank by mounting the desired head form directly on the drag balance and letting the balance and drive shaft serve as the "infinitely-long" afterbody. This set-up has already been shown in figure 3.

Three semi-infinite bodies of different shape were chosen for the MFD drag measurements. These included a classical Rankine halfbody, a 2-caliber ogive and a blunt halfbody. The head forms used for these bodies were made of lucite and their shapes and dimensions are shown in figure 6. The Rankine halfbody, which is defined by a source in a uniform stream, was an obvious choice because of the simple analytical form of its potential flow and because the magnetic field induced by the body had been measured previously by Ahlstrom (Ref. 8). Furthermore, the zero-field drag of such a body was expected to be very low so that, hopefully, the drag with field would be almost entirely MFD drag. The blunt halfbody is the simplest representative of high drag shapes and was chosen to study the effect of body shape. The choice of the ogive was originally based on the fact that it was an easily machineable streamlined shape. This was a consideration of practical importance because we had planned to make pressure distribution measurements with the drag balance which required a number of head forms of identical shape. However, due to various difficulties, these measurements were never completed. Nevertheless, we retained the ogive as a drag model since it was

available and was also representative of slightly more streamlined shapes than the Rankine halfbody.

Just as in the case of the flat disks, a tare drag measurement was also made on the semi-infinite bodies. The set-up for this measurement is also shown in figure 6 and differs from the tare drag set-up for the disks in that only the difference between the pressure acting on the upper bellows and that on the lower bellows could be measured. The unwanted force due to the decrease or increase in the pressure acting on the base of the models could not be determined directly from the tare drag measurement alone. The calculation of this "base drag" force will be described in Sec. 2.5.

2.4 Experimental Procedure

The calibration of the drag balance had to be carried out separately for each model because it varied considerably depending on the model's bouyancy in mercury. This variation was due to the non-linearity of the bellows which became significant over the very large range of the bouyancy force. However, over the much smaller load range corresponding to the expected drag forces⁴, the calibration for each model was nearly linear. The calibrations were carried out directly in the tow tank with the drag balance completely immersed in the mercury and only the very top of each model showing above the mercury surface. Some typical calibration curves for the Rankine halfbody, the blunt halfbody and the disks are shown in figure 7.

⁴ The maximum bouyancy force on a model was around 600 gm; whereas the drag forces were usually less than 100 gm.

In the series of runs for a particular model, two measurements of drag were made at each run condition. One was the measurement of the total drag which included not only the drag of the model but also other extraneous forces (see next section). The other was the tare drag measurement for which the balance set-ups described in the previous section were used. During each run, the voltage outputs from the drag balance bridge circuit and the velocity servo were displayed simultaneously on a dual-beam oscilloscope and their traces photographed with a Polaroid camera. Photographs typical of those obtained for the semi-infinite bodies are shown in figure 8. The data are for the Rankine halfbody at magnetic field strengths of 0, 3,300, 6,600 and 11,000 gauss and at a fixed velocity of about 0.3 m/sec. In all of the photographs, the upper trace is the drag balance bridge circuit output and the lower trace is the velocity servo output. The time increases from left to right. From these traces, it can be seen that the drag reaches its steady value quite rapidly and increases substantially with magnetic field.

Typical photographs of the data obtained in the non-magnetic drag measurements on the three flat disks are shown in figure 9. Identification of the upper and lower traces is the same as in the previous figure. The velocity was again fixed at about 0.3 m/sec. The interesting transient variations which can be seen in the drag traces will be discussed in detail in Sec. 3.2.

The experimental runs were made at velocities ranging from about .13 m/sec. to .9 m/sec, and for magnetic field strengths from 0 to 12,500 gauss. The corresponding ranges in the basic

dimensionless parameters were as follows:

$$3 \times 10^4 \leq Re \leq 2 \times 10^5, \quad 2 \times 10^{-3} \leq Rm \leq 1 \times 10^{-2},$$

$$0 \leq N \leq 24$$

It should also be mentioned that all the runs with magnetic field were under sub-Alfvénic flow conditions ($\alpha > 1$). The range in conditions for each particular model will be given more specifically in chapter III.

2.5 Data Reduction Procedure

It was necessary to apply certain corrections to the total measured drag of both the semi-infinite bodies and the flat disks. Some of these, such as the tare drag of the flat disks, were directly measurable; others had to be estimated or assumed. Fortunately, the corrections which were the most uncertain or arbitrary were also relatively small compared to the total drag (see Sec. 3.3). The procedure followed in determining the corrections for the data of the semi-infinite bodies will be described first.

The total measured drag of a semi-infinite body was found to consist of three parts: a base drag D_b , a viscous drag D_v and the MFD drag D_M . The first two were unwanted contributions which, if possible, we wished to separate from the total drag in order to isolate the MFD drag. The base drag was mainly due to a pressure decrease at the base of the models arising from the presence of the tow tank walls. The viscous drag was due to either skin friction, as in the

cases of the Rankine and ogive halfbodies, or to viscous dissipation in a separated wake flow, as in the case of the blunt halfbody.

The first step taken to determine those unwanted contributions was to measure the total drag of the models without the magnetic field. Prior to these measurements, the existence of the base drag was not realized and the drag was expected to be entirely viscous drag. Subsequently, however, the measured zero-field drag of the Rankine and ogive halfbodies was found to be in rather poor agreement with the theoretical laminar skin-friction drag. It was then discovered by some simple calculations that a substantial base drag could also exist which could account for the discrepancy. Therefore, before presenting the results of the zero-field drag measurements, we shall show how the base drag of the semi-infinite bodies can be calculated.

For a streamlined halfbody, such as the Rankine and ogive halfbodies, the zero-field base drag can be calculated in a very straightforward manner. The flow past the body is assumed to be inviscid and mass, momentum and energy balances are carried out on the body-fixed control volume shown in figure 10. This calculation, which is described in appendix A, yields the following value for the base drag coefficient⁵:

$$C_{D_b} = .036$$

⁵ It may seem paradoxical that a drag force is obtained in an inviscid flow, but it can be easily seen by noticing that the flow downstream (in the frame of figure 10) is accelerated to a velocity which is slightly greater than that of the uniform flow upstream. This causes a decrease in the downstream static pressure acting on the base of the model and results in a net drag force.

There is another, almost negligible contribution which may be considered as part of the base drag. This contribution was discovered through the tare drag measurements described in Sec. 2.3. In these measurements, an extremely small positive net force was picked-up by the balance, indicating that the pressure at the upper bellows was slightly greater than at the lower bellows. However, this force can actually be attributed to an increase in the overall pressure of the tow tank caused by the acceleration of mercury into the standpipe. Because the effective area of the upper bellows is slightly greater than that of the lower bellows, this pressure increase resulted in a net positive force acting on the balance. This force can be explicitly calculated (see appendix B) and gives an additional contribution of .004 to the base drag coefficient. Although the accuracy of the tare drag measurements was poor (about $\pm 30\%$) because the forces were so small, they agreed within the experimental accuracy with the calculated forces. Therefore, in the cases of the Rankine and ogive half-bodies, it was assumed that the pressure difference between the upper and lower bellows was negligible and that the zero-field base drag coefficient was given by

$$C_{D_b} = .036 + .004 = .040 \quad (2.1)$$

We mention in advance that the tare drag measurements with magnetic field gave essentially the same results; i. e., $C_D \doteq .004$, so that the pressure difference between the upper and lower bellows will also be assumed to be negligible when a magnetic field is present. This was true again of the tare drag measurements on the blunt halfbody at the

stronger field strengths (N greater than about 5), so for this body at these conditions, the same assumption will be made.

The calculation of the zero-field base drag for the blunt half-body is not nearly so straightforward. However, it can be crudely estimated and, fortunately, turns out to be a small fraction of the total drag. The calculation procedure is similar to the previous case except the drag is now assumed to be due mostly to viscous dissipation so that a dissipation term must be added to the energy balance. A pressure coefficient of $-.08$ is calculated by this procedure (see appendix C) for a point far downstream of the nose. The pressure coefficient at the lower bellows will be assumed to have this value. Now in the tare drag measurements on the blunt halfbody, positive pressure differences were always found between the upper and lower bellows which correspond to an approximately constant pressure coefficient difference of $+.05$. Therefore, the net pressure coefficient at the base must be $-.08 + .05 = -.03$, and so the base drag coefficient is just

$$C_{D_b} = +.03 \quad (2.2)$$

Having calculated the base drag coefficients, we are now ready to present the results of the zero-field drag measurements on the semi-infinite bodies. These are given in figure 11 where the drag coefficients of the Rankine, ogive and blunt halfbodies are shown plotted against the Reynolds number. The unfilled data points correspond to drag coefficients based on the total drag; whereas the filled data points correspond to the drag coefficients obtained by subtracting (2.1) from

the total drag coefficients of the Rankine and ogive halfbodies and (2.2) from the total drag coefficients of the blunt halfbody.

We first compare the filled data points of the Rankine and ogive halfbodies with the theoretical laminar skin-friction drag coefficients calculated for flat plates of the same length and surface areas as these models. These calculated coefficients are represented in figure 11 by the solid line in the case of the Rankine halfbody and by the dashed line in the case of the ogive halfbody. Although the theoretical lines appear to fall slightly below the data, the agreement is good considering that flat plate theory was used. In fact, Goldstein (Ref. 16) states that the more complicated theories for axisymmetric boundary layers usually give skin-friction coefficients which are 10 to 15 per cent above those for a flat plate. In any case, we may conclude that the boundary layer flow was laminar⁶ and assume that the skin-friction drag coefficient scales with $Re^{-\frac{1}{2}}$. The best fit to the data are then given by

$$C_{D_v} = \frac{11.3}{\sqrt{Re}}$$

for the Rankine halfbody and

$$C_{D_v} = \frac{10.0}{\sqrt{Re}}$$

⁶ This appears to be consistent with the fact that the maximum Reynolds number based on the length of the models was about 7×10^5 which is just barely above the minimum Reynolds number of 5×10^5 that is usually taken for the onset of transition.

for the ogive halfbody. The total zero-field drag coefficient can therefore be written as

$$C_{D_o} = C_{D_b} + C_{D_v} = .040 + \frac{\kappa}{\sqrt{Re}} \quad (2.3)$$

where $\kappa = 11.3$ for the Rankine halfbody and 10.0 for the ogive halfbody. This equation is plotted in figure 11 and can be seen to fit the data very well.

The drag coefficients of the blunt halfbody corresponding to the uppermost filled data points in figure 11 remain to be considered. There is no theory with which these drag coefficients can be compared, but their average value of 0.66 compares very well with the experimental value of 0.65 given in Ref. 14 for the forebody drag coefficient of a blunt halfbody. In fact, this average value is not too far from the value of 0.72 obtained by subtracting the base pressure coefficient of a flat disk from its total drag coefficient (Ref. 17). Thus, the measured drag for the blunt halfbody appears to be fairly well substantiated.

Now that we have established that the total zero-field drag of the halfbodies consists of a base drag and a viscous drag, we must consider next the determination of these quantities when the magnetic field is present.

For the Rankine and ogive halfbodies, we simply assume that the base drag and viscous drag at any field strength is given by

$$C_{D_b} + C_{D_v} = C_{D_o}$$

where C_{D_o} is just the total zero-field drag coefficient given by eqn.

(2.3). For $N < 1$, this should be a very good assumption since the flow should only be slightly disturbed from zero-field flow conditions (also see discussion in Sec. 4.1). In particular, the base drag and viscous drag should be little affected. For $N > 1$, the assumption is admittedly somewhat arbitrary, but some justification can be given. First of all, we show in appendix C that the base drag coefficient, C_{D_b} , must increase as N increases. However, it cannot become greater than a value of .107, which is about equal to the maximum zero-field drag, C_{D_0} . Secondly, in appendix D we show by an order-of-magnitude analysis of the equations of motion that the ordinary viscous boundary layer equations should describe the boundary layer flow under the conditions of the present experiments. If this is true, then the skin-friction drag coefficient, C_{D_v} , should decrease as N increases because the flow velocity at the outer edge of the boundary layer is decreasing due to the development of a vortical wake which will be described in chapter IV. It is also shown in chapter IV that a stagnant region must develop in front of the bodies as N increases, which should further reduce the skin-friction drag. Thus, if C_{D_b} increases and C_{D_v} decreases as N gets larger, then it is possible that the sum of the two quantities may remain approximately constant and equal to C_{D_0} . In any case, in the absence of even an approximate theory by which these quantities could be calculated, this appeared to be the most logical assumption to make in attempting to isolate the MFD drag. Moreover, at the higher values of N where the assumption may be questioned the most, the uncertainty in the quantities was only a small percentage (around 5 per cent) of the MFD drag. Consequently,

the drag coefficients for the Rankine and ogive halfbodies were based on the MFD drag assumed to be obtained by subtracting the total zero-field drag from the total drag with field.

For the blunt halfbody, it is not only impossible but also illogical to attempt to separate the viscous drag from the MFD drag. The two drag forces are undoubtedly closely coupled in this case since even a small magnetic field could have large effects on the viscous drag by affecting the stability or turbulence level of the wake. The calculation of such an interacting flow is unlikely to be accomplished in the near future. Therefore, no attempt was made to separate the viscous drag from the MFD drag, and instead, the drag coefficients for this body were based on the total drag minus a small base drag correction. This base drag was calculated in the same way as the zero-field base drag (see appendix D). Since the total drag increased only slightly (c. f. , Sec. 3.1), the pressure coefficient at the lower bellows was assumed to be the same as in the zero-field case; i. e. , $C_p = -.08$. The base drag was then calculated by adding to this the difference between the pressure coefficients at the upper and lower bellows as obtained by the tare drag measurements. We mentioned earlier that this difference became negligible at the stronger fields so that for these conditions, $C_{D_b} \rightarrow +.08$.

We must finally consider the procedure followed in reducing the flat disk data. The procedure in this case was trivial compared to the previous cases. It simply consisted of subtracting the measured tare drag from the measured total drag. No corrections were made for possible wall blockage effects since it was the time

dependence of the drag that was mainly of interest and not its absolute magnitude. The data were also not corrected for the inertia forces produced during the initial acceleration period because the measurements were not considered reliable at these very early times. The data from this period, which constituted only a small fraction of the total data since acceleration occurred only during the first 2 to 3 inches of travel, were disregarded.

III. RESULTS OF THE EXPERIMENTS

3.1 MFD Drag of Semi-Infinite Bodies

The results of the drag measurements on the semi-infinite bodies are presented in figure 12 where the drag coefficients of these bodies are plotted as functions of the interaction parameter for various values of the Reynolds number and magnetic Reynolds number. As discussed in Sec. 2.5, the drag coefficients of the Rankine and ogive halfbodies were based on the MFD drag; whereas, the drag coefficients of the blunt halfbody were based on the sum of the MFD drag and viscous drag. The error bars on the data points at the higher values of N will be explained in Sec. 3.3.

The drag coefficients of all three bodies are seen to correlate to within the experimental scatter in the data with N alone. There appears to be no systematic dependence on the Reynolds number or magnetic Reynolds number¹. This correlation with N was not unexpected since it was strongly suggested by the equations of motion presented earlier in chapter I and also by other theoretical considerations to be discussed in chapter IV.

Moreover, such a correlation had been found previously by Yonas (Ref. 10). The main result of his experiment, which was briefly described in the Introduction, was that the drag coefficients of both the sphere and the flat disk increase monotonically from their zero-field values as a function of N only. This increase was found to

¹ It should be noted that the ratio, $Rm/Re = \mu\sigma\nu$, is a constant fixed by the properties of the fluid so that one of these parameters could not be varied independent of the other.

be negligible for $N < 1$, but for larger values of N ($N > 10$ for the sphere and $N > 20$ for the disk) the increase was found to be proportional to \sqrt{N} .

Our results corroborate Yonas' conclusion that N is the principal correlation parameter, but the dependence of the drag coefficients on N found by us differs markedly from that found by him. We shall discuss some of the reasons for the difference in behavior in chapter IV.

For the Rankine and ogive halfbodies, the dependence of the MFD drag coefficients on N may be divided into two regions of behavior. Over the range, $0 \leq N < 2$, the dependence on N is linear to within the experimental error of ± 25 per cent². This may be seen by comparing the data with the three lines proportional to $N^{\frac{1}{2}}$, N and $N^{1.5}$ which have been plotted on figure 12. The mean trend of the data is unmistakably best represented by the linear line. For values of N greater than 2, the dependence on N becomes quite nonlinear. The rate of increase of the drag coefficients is seen to diminish rapidly as N increases and at the higher values of N , they appear to be leveling off to some asymptotic value. In chapter IV, it is suggested that the drag coefficient of any halfbody must reach a limiting value of unity and this trend is definitely evident in the behavior of the data.

² This error may seem rather high, but it can arise because the drag coefficients were based on the difference between two drag measurements. For $N < 1$, this difference was relatively small so that its relative error was much larger than the error in the measurements (also see Sec. 3.3).

For the blunt halfbody, the dependence of the drag coefficient on N is seen to be very slight. The maximum increase in C_D is only about 25 per cent. This behavior was in fact anticipated³ since the drag without field was around 0.7 and, as mentioned above, was expected to increase to a value of 1 at most. However, we should point out that this expectation is based on the assumption that the drag of the halfbody becomes entirely MFD drag and that the viscous drag due to separated flow vanishes as $N \rightarrow \infty$. Some support for this assumption is provided by the fact that the drag coefficients of all three halfbodies appear to be converging at the higher values of N . Since it is reasonable to assume that the MFD drag of the blunt halfbody was of the same order as the MFD drag of the Rankine and ogive halfbodies at these higher values of N , this implies that the viscous drag of the blunt halfbody was becoming very small.

Before concluding this section, we feel compelled to remark that the correlation with N in figure 12 may appear deceptively obvious since this was the only form in which the data was presented. The extent to which the correlation succeeds may have been better appreciated had we plotted the data in a different form first. As an example, we have taken the MFD drag coefficients of the Rankine halfbody and have plotted them in figure 13 against the Reynolds number at various Hartmann numbers. This closely corresponds to the form in which the data was originally obtained; i. e., with the increase in drag plotted

³ This accounts for the fewer data points plotted for this body. Only enough measurements sufficient to establish this rather uninteresting behavior were made.

against the velocity at various field strengths. We can now see more clearly what the correlation accomplishes. It is essentially this: Each horizontal line, $C_D = \text{constant}$, in figure 13 is transformed by the correlation into a single point on the curve for the Rankine halfbody in figure 12.

3.2 Drag of Impulsively-Started Flat Disks

The data obtained from the non-magnetic drag measurements on the flat disks are offered here simply as preliminary experimental findings of an interesting flow phenomena. We will attempt no theoretical analysis of the flow, but we will discuss some qualitative ideas about the nature of the flow.

Results are first presented in figure 14 from the drag measurements on the three disks of 1.0, .75 and .50 in. diameter taken at a fixed velocity of .30 m/sec. The traces for these measurements were shown earlier in figure 9. For reasons discussed in Sec. 2.5, data are not plotted for the initial acceleration period. In the upper half of the figure, the data for the three disks are given essentially in their raw form with the drag balance output in millivolts plotted against the time in seconds. The drag amplitudes of the three disks and the times at which changes in these amplitudes occur are seen to differ considerably. In the lower half of the figure, the drag has been converted into a drag coefficient and plotted against the time divided by the characteristic time, d/U . The three drag curves scaled in this way can now be seen to correlate fairly well.

In order to show that this correlation holds over a fairly wide range of Reynolds number, results are presented in figure 15 from the drag measurements on the .75 in. diameter disk taken over a Reynolds range of 2.2×10^4 to 1.2×10^5 . Data points rather than continuous curves have been used to plot the drag coefficients in this figure so that the runs at the different Reynolds numbers can be distinguished. Although considerable variation in the data can be seen, there appears to be no systematic dependence on Reynolds number.

A number of interesting features may be observed in the time-dependent behavior of the drag coefficient. After the initial acceleration period, it appears to be decreasing from some higher level and drops to a minimum value of about 1.0 at around $Ut/d = 6$. It then increases to a maximum value lying between 1.5 and 1.8 at around $Ut/d = 15$ before decreasing again to its steady-state value. For the 1.0 and .75 in. diameter disks, the steady-state value lies somewhat above the accepted standard value of 1.17 given in Ref. 14, but this discrepancy can be accounted for by the blockage effect of the tow tank walls. It should finally be observed that the steady-state value is not reached until the disk has traveled a distance equal to about 25 times its diameter (since Ut is approximately the distance traveled). This is a surprisingly long distance and it is probably much longer than intuition would lead most people to expect.

The above results appear to be the first to the author's knowledge for the time-dependent drag of an axisymmetric body in an

impulsively-started flow. However, a number of other investigators have found similar results in closely-related experiments.

Schmidt (Ref. 18), in a very early experiment (1919), measured the acceleration velocities of freely-falling spheres in water and of free-rising balloons in air. His results for three of the spheres, for which terminal velocity was reached, have been plotted (after non-dimensionalizing the velocities with the terminal velocity, U_t , and the time with d/U_t) along with the drag data in the lower part of figure 15. The first maximum in the velocity can be seen to occur at about the same time that C_D reaches its minimum. Conversely, the minimum in the velocity occurs at about the same time that C_D reaches its maximum. Furthermore, the time (scaled with d/U_t) required to attain steady-state is also about the same; i. e., $U_t t/d = 25-30$. This close correlation between the results of the two experiments indicates that the development of the flow may have been nearly the same in both.

In another early experiment (1935) conducted by Schwabe (Ref. 19), the time-dependent drag of a two-dimensional circular cylinder was determined. He used an indirect method in which the velocities and pressures were successively calculated from photographs of the flow taken at many stages of development. His results showed that the form-drag coefficient (skin-friction not included) of the cylinder increased monotonically with time to a value of 2.07 at $Ut/d = 4.5$, which is considerably above its steady-state value of about 1. The drag was not determined beyond $Ut/d = 4.5$.

Finally, in a very recent experiment (1966), Sarpkaya (Ref. 20) made direct measurements of the time-dependent drag of two-

dimensional circular cylinders and flat plates. The duration of his experiments was long enough so that steady-state was reached. His results for the circular cylinders showed that the drag coefficients increased initially very much like Schwabe's, but at $Ut/d = 4$ it reached a maximum value of about 1.54 and then slowly decreased to its steady-state value. More relevant to our results are his measurements on the flat plates which were taken over a range of Reynolds numbers from 1.5×10^4 to 1.1×10^5 , which is nearly the same range as ours. The drag coefficient calculated from these measurements is represented by the shaded curve plotted in figure 15. The drag coefficient amplitudes of the flat plates are seen to be about twice those of the flat disks, but the time-dependent behavior of the drag coefficient is seen to be very similar. The minimum and second maximum for both occur at approximately the same times.

Sarpkaya also made detailed visual flow studies of the development of the vortices behind a flat plate and was able to correlate the various stages of their development with the changes in drag. He found that the flow was potential flow initially, but shortly after the start of the motion separation occurred and a pair of symmetrical vortices began to grow behind the plate. During this period of growth, which evidently extended up to the time C_D reached its minimum, the drag is thought to be due mainly to the energy consumption required for the enlargement of the vortices. Shortly after the minimum C_D was reached, the vortices were observed to become unsymmetrical and this apparently caused the drag to increase again until the second maximum in C_D was reached. This maximum C_D was found to

correspond with the shedding of the first vortex. Subsequently, the drag decreased and underwent a number of oscillations before finally reaching its steady-state value. Each one of the peaks in these oscillations was found to correspond to a shedding of another vortex.

A similar series of events may also take place during the development of the vortices behind a flat disk. This is suggested not only by the similarity in the time-dependent behavior of the drag coefficients, but also by some visual flow studies carried out by Schmidt (Ref. 18) in conjunction with his experiment described above. From these observations, he was able to determine that a falling sphere reached its minimum velocity (maximum C_D) at the same time that the first vortex ring (vortex pair at cylinder) separated from the sphere, which corresponds exactly with Sarpkaya's observation. Of course, it is not strictly correct to compare two-dimensional flows with axisymmetric flows because the vortex structure is known to be much more complex in axisymmetric flows (Ref. 21). Nevertheless, there is certainly strong evidence for believing that the growth and shedding of vortices have about the same general effect and occur on about the same time scales in the two flows.

There is one other curve plotted in figure 15 which has not been discussed yet. This is the curve designated "Theory of Fromm and Harlow" which appears to compare rather well with the drag coefficient of the flat disk. Unfortunately, this agreement is entirely fortuitous. The curve is the result of extensive computer calculations by Fromm and Harlow (Ref. 22) for two-dimensional flow past a flat plate, and thus should actually be compared with Sarpkaya's data.

However, the agreement with Sarpkaya's data is poor and is attributed by Sarpkaya to the fact that Fromm and Harlow's result is for a Reynolds number of 300 which is much lower than the Reynolds numbers of the experiment. Nevertheless, the calculated drag coefficient does show very similar variations with time. Moreover, the calculated streamline patterns showed that the vortices develop in essentially the same way that was observed experimentally by Sarpkaya. Thus, it would appear that the results of the numerical calculations are reasonably in accord with the experimental observations.

It is difficult to say at this time what practical significance, if any, our results will have. They undoubtedly will have some relevance to the motion of any rapidly-accelerated body for which a separated wake develops. One example is the commonly-performed experiment in which the drag of a body is measured by letting the body rise or fall freely and timing its rate of ascent or descent. Our results indicate that serious errors may be incurred if the measurements are made too early. We might also mention here that the time-dependent drag coefficient of the two-dimensional circular cylinder has been used to calculate the force coefficients of slender bodies at angles of attack in steady subsonic to moderately supersonic flows (Ref. 20). In such calculations it is assumed that the development of the crossflow along the slender body is analogous to the development with the time of the flow past a cylinder which has been started impulsively in motion. However, there appears to be no such analogy appropriate to the axisymmetric case.

3.3 Discussion of Uncertainties

The uncertainties which pertain to all the measurements in general will be summarized first. For the directly measured quantities, the average uncertainties were as follows:

Velocity, U	± 3%
Magnetic Field, B ₀	± 1%
Drag Balance Calibration	± 2%

There were also uncertainties in the values of the fluid properties which entered into the computation of the interaction parameter. These are the density, ρ , and the electrical conductivity, σ , and their values for mercury were taken as (Ref. 23):

$$\rho = 13.5 \times 10^3 \text{ kg/m}^3$$
$$\sigma = 1.04 \times 10^6 \text{ mhos/m}$$

Some variations in these values occurred due to temperature changes of up to 30-40°F caused by the heating of the magnet. This resulted in an uncertainty in the ratio σ/ρ of about ± 2%. The combination of all of the above uncertainties leads to an average uncertainty in the drag coefficient of ± 6% and an average uncertainty in the interaction parameter of ± 4%.

The uncertainties which pertain only to measurements in a particular range of N will be discussed next. First of all, we shall estimate the uncertainty in the MFD drag coefficients of the Rankine and ogive halfbodies for $N \leq 1$. These drag coefficients were based on the difference between two drag measurements; i. e., on $C_D - C_{D_0}$.

Now since $C_D - C_{D_0}$ was only about 25-30% of C_D for $N \leq 1$ and since the individual uncertainties in C_D and C_{D_0} were $\pm 6\%$, the uncertainty in $C_D - C_{D_0}$ must have been about $\pm 20-25\%$. This is approximately the order of the scatter in the data of figure 13 for $N \leq 1$.

Secondly, we must explain the uncertainties associated with the error bars on the data points for $N > 10$ in figure 12. These uncertainties arose because the drag did not level-off to a constant value at these higher values of N , but continued to decrease very slightly (5-10%) throughout a run. This decrease, which is given by the length of the error bars, is attributed to the interaction of the small displacement flow caused by the drive shaft entering the tow tank⁴ with the fringing magnetic field near the top of the tank. Because of this interaction, the velocity profile of the displacement flow becomes quite peaked near the axis of the tow tank⁵. This peaked velocity profile could extend down the tank for some distance at high field strengths. Consequently, as a model moves upward in the tank, it effectively sees the velocity upstream decreasing, thus accounting for the decrease in drag. The uncertainty due to this effect was probably on the order of $\pm 6\%$.

⁴ Since the ratio of the cross-sectional area of the tank to that of the drive shaft is 30:1, the mean velocity of this displacement flow is 1/30 the velocity of the shaft.

⁵ Such an effect has been observed by Maxworthy (Ref. 24) in a liquid sodium tunnel. Some very preliminary velocity measurements in the tow tank taken by Mr. B. M. Lake (Ref. 25) also give some evidence for this.

Finally, we must mention the effect of the magnetic field on the drag balance. Although all parts of the balance were made of supposedly non-magnetic stainless steel (Type 303 or 304), they were still very slightly magnetic. Therefore, a small force was picked-up by the balance as it passed through the fringe field near the bottom of the tow tank. This force was measured by running the balance through the fringe field at a very slow speed. For $N > 10$, the correction to the drag for this effect is estimated to result in an additional uncertainty of $\pm 4\%$.

Thus, the total uncertainty in the drag coefficients for $N > 10$ is estimated to be about $\pm 9\%$.

IV. THEORETICAL DISCUSSION

In chapter I, the general equations were considered for the flow of an incompressible, viscous and electrically conducting fluid past an axisymmetric body in an aligned magnetic field. For the limiting case, $Rm \rightarrow 0$, and $Re \rightarrow \infty$, corresponding to an inviscid, slightly conducting fluid, these were reduced to the following equations:

$$\frac{\partial u}{\partial x} + \frac{\partial v}{\partial r} + \frac{v}{r} = 0 \quad (4.1a)$$

$$u \frac{\partial u}{\partial x} + v \frac{\partial u}{\partial r} = - \frac{\partial p}{\partial x} \quad (4.1b)$$

$$u \frac{\partial v}{\partial x} + v \frac{\partial v}{\partial r} = - \frac{\partial p}{\partial r} - Nv \quad (4.1c)$$

The induced magnetic field for this limiting case was shown to be negligibly small and the magnetic field was everywhere taken to be equal to the uniform applied field. In this chapter, solutions to eqns. (4.1) will be considered for the two special cases of (1) weak interaction between the flow and magnetic field, $N \ll 1$, and (2) strong interaction between the flow and the magnetic field $N \gg 1$. Since N is proportional to B_0^2/U , the first case can exist either for weak magnetic fields or high velocities, and the second for strong magnetic fields or low velocities.

4.1 Weak Interaction Case, $N \ll 1$

In this case, to zeroth order in N , the magnetic force term in eqns. (4.1) may be neglected in comparison with the inertia force

terms. The equations then reduce to the classical hydrodynamic equations for an inviscid fluid. Thus, to a first approximation, the flow past a body can be simply assumed to be potential flow.

Under this assumption, a rather simple first-order calculation can be made of the MFD drag of the body. The method of calculation is based on the first law of thermodynamics in accordance with which the work done on the fluid by the drag force per unit time is equated to the energy dissipated by Joule heating per unit time; i. e. ,

$$DU = \int_{V^*} \frac{j^{*2}}{\sigma} dV^* \quad (4.2)$$

where V^* is the total volume occupied by the fluid. Now the current density is given by Ohm's law:

$$\underline{j}^* = \sigma(\underline{q}^* \times \underline{B}^*)$$

But in the present approximation, \underline{q}^* is to be taken as the potential velocity, \underline{q}_0^* , and \underline{B}^* as the undisturbed uniform applied field, $-B_0 \underline{i}$, so that the current density is just

$$j^* = \sigma B_0 v_0^* \quad (4.3)$$

where v_0^* is the radial component of the potential velocity. In general, for a body of characteristic dimension d in a uniform flow of velocity U , v_0^* may be written in the form:

$$v_o^*(\underline{x}) = U v_o(\underline{x}) \quad (4.4)$$

where $\underline{x} = \underline{x}^*/d$. Substitution of (4.3) and (4.4) into (4.2) leads to

$$C_D = \frac{D}{\frac{1}{2} \rho U^2 \pi(d^2/4)} = \frac{8}{\pi} N \int_V v_o^2(\underline{x}) dV, \quad (4.5)$$

where $N = \sigma B_o^2 d / \rho U$ and $dV = dV^*/d^3$.

Note that according to (4.5) the drag coefficient increases linearly with N as long as v_o is independent of N , which it obviously is for potential flow. However, (4.5) also gives the Joule-loss contribution to the drag for inviscid, small Rm flows at arbitrary N ; but in this case v_o may be a function of N . The integral of (4.5) should be convergent for all potential flows past bodies, but Liepmann (Ref. 26) has noted that it is divergent in the case of Stokes flow past a sphere.

The weak-interaction theory described above appears to have been first applied by Chopra and Singer (Ref. 27). They used the Joule-loss method to calculate the drag of a uniformly magnetized sphere and of a sphere of finite conductivity in a uniform external field for both translational and rotational motions. However, subsequently, Reitz and Foldy (Ref. 28) pointed out that some of Chopra and Singer's results were in error due to their neglect of induction effects within the sphere and rederived the correct expression for the drag. Furthermore, they also carried out a complete first-order perturbation solution of the inviscid MFD equations (including perturbations of the magnetic field) for the case of a sphere moving

parallel to a uniform applied field and showed that the drag calculated directly from the perturbed pressure distribution was the same as that calculated from the Joule-loss method. One other calculation that deserves mention is that of Ludford (Ref. 29) who used the Joule-loss method to calculate the drag of a sphere having an internal dipole field.

Although the weak-interaction theory based on the Joule-loss method leads to a simple calculation for the MFD drag, it is a valid approximation only for small N flows which are closely described by a potential field. It certainly cannot be applied to flows past bluff bodies at high Reynolds numbers since the separated flow behind such bodies is not describable by potential flow theory and in some flow regimes may be strongly affected by even small magnetic fields. This would appear to be the main difficulty with the various cases of MFD flow past a sphere treated in the above-mentioned papers. However, there are at least two physically realizable cases for which the theory should be valid and we shall discuss these next.

One case is that of a sphere which is rapidly oscillating parallel to a uniform applied magnetic field. This was the case that was studied both theoretically and experimentally by Motz (Ref. 9) whose experiment was briefly described in the Introduction. The oscillation frequency of the sphere in this experiment was sufficiently high to justify using the potential velocity field to describe the bulk motion at small N . As one would expect, the drag amplitude calculated by Motz by the Joule-loss method has the same value as the drag calculated by Reitz and Foldy for the steady motion of a sphere. Motz also calculated second and third-order corrections to the drag using a

formula derived by Ludford and Murray (Ref. 30) for the steady motion of a sphere¹. He found excellent agreement between this third-order calculation and his measured drag. Both his theory and data departed from linear behavior at an equivalent² N of about 0.1 and are about 30 per cent lower than the linear theory at an equivalent N of 0.3.

The other case which should be describable by a potential field is the small N flow past a streamlined semi-infinite body. In particular, such a description should be valid for the ogive and Rankine halfbodies which were used in the present experiments. The results of the zero-field drag measurements presented in Sec. 2.5 indicated that the flow past these bodies was very close to potential flow. The calculation of the drag coefficient by the Joule-loss method is easily carried out in the case of the Rankine halfbody since its potential field is given simply by a source in a uniform stream. On the other hand, there is no simple analytical expression for the potential field of the ogive halfbody and this precludes a calculation of its drag coefficient. However, it was seen in figure 12 that the MFD drag coefficient for this body exhibits the linear behavior predicted by eqn. (4.5).

¹ There are several points about this analysis which are quite unclear to the present author. For example, it does not appear at all obvious that Ludford and Murray's drag formula for steady flow can be applied without modification to periodic flows. There also appears to be an inconsistency in the derivation of the higher-order equations governing the velocity fields. In particular, the complete neglect of the convection terms and the magnetic field perturbations does not appear justifiable for the third-order calculation.

² Motz defines the interaction parameter as $N = \sigma B_0^2 / \rho \omega$ where ω is the frequency in rad/sec.

The radial velocity for potential flow past a Rankine halfbody is given by

$$v_o = \frac{1}{16} \frac{r}{(x^2 + r^2)^{3/2}}$$

where the cylindrical coordinates, x and r , have been nondimensionalized by the asymptotic body diameter, d (see figure 10). Substitution of the above expression into (4.5) gives

$$C_D = \frac{N}{32\pi} \left[\int_{-\infty}^{-\frac{1}{4}} dx \int_0^{\infty} \frac{2\pi r^3 dr}{(x^2 + r^2)^3} + \int_{-\frac{1}{4}}^{\infty} dx \int_{r_b}^{\infty} \frac{2\pi r^3 dr}{(x^2 + r^2)^3} \right] \quad (4.6)$$

where the body radius, r_b , is a transcendental function of x defined by (Ref. 31)

$$r_b = \frac{1}{8} [1 + x(x^2 + r_b^2)^{-\frac{1}{2}}]$$

Also note that $r_b = 0$ at $x = -\frac{1}{4}$. Integration of (4.6), which requires numerical evaluation of the integral involving r_b , leads to the following result:

$$C_D = 0.200 N \quad (4.7)$$

This result has been plotted in figure 16 as a dashed line and can be compared with the data for the Rankine halfbody which have been replotted in this figure from figure 12. The theoretical line can be seen to lie somewhat above the data (about 15-20 per cent), but this discrepancy may be attributed to the presence of the tow tank walls. If the integrals in (4.6) are evaluated only out to the radius,

$r = r_w = 2.75$, of the tow tank instead of to infinite radius, the proportionality constant is reduced by about 13 percent and the equation for the drag coefficient becomes

$$C_D = 0.173 N \quad (4.8)$$

This equation, which is the solid line plotted on figure 16, shows fairly good agreement with the data, although it may still be about 5 percent higher than the mean of the data. Even this small discrepancy could probably be accounted for if a correction were made for the fact that the radial velocities given by eqn. (4.6) do not vanish at the tow tank walls. Although these velocities are very small ($v_{o \max} = .008$ at $r = r_w$), this correction may possibly reduce the drag coefficient by another few percent. However, such a correction was not calculated because it was found to involve evaluation of a volume integral of integrals of elliptic functions which would have required extensive computations even on a computer.

In any case, in view of the scatter in the data, the agreement of eqn. (4.8) is sufficiently close so that it can be concluded that the validity of the weak-interaction theory based on the Joule-loss method has been verified. Moreover, the main consequence of the theory was the linear increase of the drag coefficient with N , and this predicted behavior is fully confirmed by the data of both the ogive and Rankine halfbodies at small values of N .

The verification of the weak-interaction theory for $N \ll 1$ is hardly surprising since the theory is very straightforward and no gross

assumptions were made. What is surprising is the apparent agreement of the data with this linear theory over a range of N which appears to extend almost up to $N = 2$. From eqn. (4.5), we would expect to see C_D increase more slowly with N for values of N of $O(1)$ since the radial velocities must be appreciably reduced for these conditions by the magnetic force. However, a very plausible explanation can be given for the observed behavior of the data. Most of the important physical and theoretical concepts underlying this explanation were found in a paper by Tamada (Ref. 32). Since his work also offers considerable insight into MFD flows in general, it will be discussed first.

Tamada considered the theoretical problem of flow past a two-dimensional circular cylinder for the special limiting case: $R_m \rightarrow 0$, $\alpha^2 \rightarrow \infty$ and $N \ll 1$. The equations used by him for this problem are identical to eqns. (4.1). His method of solution was to solve the vorticity equation, obtained by taking the curl of the momentum equation, by expanding \underline{q} and the vorticity, ω , as power series in N . The most significant feature of his first-order solution was a nondiffusive vortical wake which he found existed downstream of the cylinder. His result³ for $N = .4$ (based on cylinder diameter) is illustrated in figure 17. The most important point to note about this wake is that its profile neither widens nor dissipates, but remains fixed in shape as it travels downstream. At the same time, the pressure and transverse velocity decay to zero.

³ A similar result was found by Leonard (Ref. 33) from a numerical solution of the same problem.

Although such a solution may at first sight appear physically unacceptable because of the nonuniformity at downstream infinity, it becomes reasonable when one considers the effect of a small viscosity. As Tamada pointed out, this agency will ultimately diffuse the wake so that eventually uniform flow conditions will be regained far downstream. However, at high Reynolds number, the action of viscosity takes place over a very long distance so that its effect near the body may be ignored.

One may also question why such a wake should develop in the first place. Tamada answered this question by considering a generalized Bernoulli law for inviscid, MFD flows. This law may be obtained by rewriting eqn. (1.1b) in the form:

$$\nabla\left(\frac{1}{2}q^2 + p\right) - \underline{q} \times (\nabla \times \underline{q}) = N(\underline{j} \times \underline{B})$$

Taking the scalar product of this equation with \underline{q} gives

$$\underline{q} \cdot \nabla H = N \underline{q} \cdot (\underline{j} \times \underline{B}) = -N \underline{j} \cdot (\underline{q} \times \underline{B}) = -N j^2 \quad (4.9)$$

where $H = \frac{1}{2}(u^2 + v^2) + p$. Since $\underline{q} \cdot \nabla H$ is the change of H along a streamline and $j^2 > 0$, the above relation states that H can only decrease along a streamline. What this means physically is that the kinetic energy of a fluid particle is being dissipated by Joule heating; and since the fluid is assumed inviscid, this energy cannot be recovered by energy transfer from adjacent fluid particles.

If we now specify that $p = v = 0$ and $u = 1$ at $x = -\infty$ (upstream infinity), which is a physically reasonable assumption for

finite N and R_m , then eqn. (4.9) requires that

$$\frac{1}{2} (u^2 + v^2) + p < \frac{1}{2} \quad (4.10)$$

along all streamlines where $j \neq 0$. If we further specify that $p, v \rightarrow 0$ as $x \rightarrow +\infty$ (downstream infinity), then we see immediately from this inequality that the downstream vortical wake in question is inevitable. In fact, this vortical wake is not unlike the rotational flow which develops behind a curved bow shock in inviscid, compressible flows.

At this point, it should be noted that eqns. (4.9) and (4.10) are rather general results which were derived for arbitrary N and $R_m (< \infty)$ for both two-dimensional and axisymmetric flows with aligned fields. We shall have occasion to refer to these results again in the next section when they are applied to the case $N \gg 1$.

It is clear that Tamada's results presented above are also directly applicable to the case under consideration; i. e., to the flow past a semi-infinite body. Here, too, a nondiffusive, vortical wake can be expected to exist far downstream. The main consequence of this, as pointed out by Childress (Ref. 34), is that the vortical wake must now be taken into account when calculating momentum and energy balances. As an explicit example, we shall reconsider the energy balance that led to the result given by eqn. (4.5).

We choose a control volume which moves at steady velocity U with the halfbody but is viewed from a frame which is at rest with respect to the fluid at $x = -\infty$ (see figure 18a). The surfaces of this control volume are taken to be at large distances from the nose of the halfbody, and we assume that outside the vortical wake the flow

perturbations decay sufficiently fast with distance from the nose such that they contribute negligibly to the energy flux through these surfaces. This assumption will be examined in more detail below. Following Childress (Ref. 34), we define a non-negative wake function, $F(r;N)$, such that

$$\underline{q}^* \rightarrow U(1 - F) \underline{i} \quad \text{as } x^* \rightarrow \infty, r^* \text{ fixed}$$

Now the first law of thermodynamics states that

$$W = Q + \Delta E$$

where W is the work done on the fluid per unit time, Q is the heat transferred from the system per unit time and ΔE is the change in the internal energy of the system per unit time. For the present flow system, W is just the work done by the drag force, Q is the Joule dissipation and ΔE is the kinetic energy which is transferred out of the control volume via the vortical wake. Therefore, the first law may be written as

$$DU = \int_{V^*} \frac{j^{*2}}{\sigma} dV^* + \int_{S^*} \rho U(1-F) \frac{(UF)^2}{2} dS^*$$

where V^* is the volume occupied by the fluid within the control volume and S^* is the interval, $d/2 \leq r^* \leq \infty$ at $x^* \rightarrow \infty$. This equation may be rewritten in the following dimensionless form:

$$C_D = \frac{8}{\pi} N \int_V j^2 dV + \frac{8}{\pi} \int_S (1-F) \frac{F^2}{2} dS \quad (4.11)$$

where $dV = dV^*/d^3$, $dS = dS^*/d^2$ and S is the interval $\frac{1}{2} \leq r \leq \infty$,
 $x \rightarrow \infty$.

Thus, we see that an additional term due to the vortical wake now appears in the equation for the drag coefficient⁴. Since $F \leq 0$, this term always gives a positive contribution to C_D . In fact, it is just this contribution which may account for the observed linear behavior of C_D even for values of N of $O(1)$. What is postulated here is that although the dependence of the Joule-loss term on N is decreasing, this decrease is just balanced by an increasing contribution from the wake term. Consequently, the drag coefficient continues to increase linearly with N^5 . It would be interesting to calculate the wake contribution for Tamada's result at $N = .4$ which was shown in figure 17. An approximate integration of his calculated wake function shows that the wake term is about 9 percent of the first-order Joule-loss term.

For $N \ll 1$, the Joule-loss term is much larger than the wake term so that we were justified in omitting the latter term in eqn. (4.5). In order to show this in general, it will be convenient to derive another expression for the drag which is strictly in terms of the function F . For this purpose, a momentum balance is considered; this time in a frame fixed to the halfbody as shown in figure 18b. Again we assume that the flow perturbations far away from the nose of

⁴ We might note that if viscosity were introduced into the problem, this term would vanish but an additional viscous dissipation term would have to be added.

⁵ This could possibly be checked experimentally by measuring the velocity field in the wake to determine F .

the body and outside the vortical wake contribute negligibly to the momentum flux. Note that in order to conserve mass, there must be a mass flux through the sides of the cylindrical control volume. A momentum balance then gives

$$D = \rho U^2 \int_{x^*=-\infty}^{R \rightarrow \infty} (2\pi r^*) dr^* - \frac{\pi}{4} d^2 \rho U^2 - \rho U^2 \int_{x^*=+\infty}^{R \rightarrow \infty} (2\pi r^*) F dr^* - \rho U^2 \int_{x^*=+\infty}^{R \rightarrow \infty} (2\pi r^*) (1-F)^2 dr^*$$

Or in dimensionless form⁶,

$$C_D = \frac{8}{\pi} \int_S (1-F) F dS \quad (4.12)$$

Subtracting this from eqn. (4.11) gives

$$N \int_V j^2 dV = \int_S (1-F) (F - \frac{1}{2} F^2) dS \quad (4.13)$$

Now the first-order Joule-loss term gives $C_D \propto N$ for $N \ll 1$, But then eqn. (4.13) requires that $F \propto N$. Therefore, the wake term in eqn. (4.11) must be of order N^2 and the ratio of this term divided by the Joule-loss term must approach zero as $N \rightarrow 0$.

The results obtained above, in particular eqns. (4.11) and (4.12), are general expressions⁷ which hold for arbitrary, though

⁶ Note that the same result is applicable to ordinary viscous flows. However, in this case F is the velocity defect due to viscous dissipation and changes its form as the wake widens downstream.

⁷ By redefining S to be the interval $0 \leq r \leq \infty$ at $x \rightarrow \infty$, these same expressions may be applied to axisymmetric closed bodies.

finite, values of N provided the assumptions invoked in deriving them are valid. Since these results are relevant not only to the foregoing discussion but also to the discussion in the next section, we shall examine the assumptions in detail. The major assumptions were the following: (1) the flow is inviscid, (2) $p^*, v^* \rightarrow 0$ as $x^* \rightarrow \infty$ and (3) the flow perturbations outside the vortical wake decay sufficiently fast with distance from the nose of the body such that they contribute negligibly to the energy and momentum fluxes at infinity⁸.

Some support for the first assumption is provided by the experimental results which have shown that C_D is only a function of the strictly inviscid parameter, N . The assumption is also physically reasonable if the Reynolds number of the flow is high and there is no separation. These conditions are certainly satisfied for flow past streamlined halfbodies, and the data for the blunt halfbody (c. f., Sec. 3.1, p. 30) indicate that they may also be satisfied for bluff halfbodies at high N . In the case of flow past bluff closed bodies at high N , the inviscid flow assumption raises some subtle questions which will be discussed in connection with assumption (2).

We would certainly expect the second assumption to be a physically reasonable one for any real flow which includes viscosity. However, Yonas (Ref. 10) has shown that a strictly inviscid flow analysis cannot satisfy this assumption and still be compatible with the results of his measurements (c. f., Sec. 3.1) which showed that a

⁸ Note that we have taken the freestream pressure to be zero. This is convenient since the drag is always measured with reference to the freestream pressure.

stagnant region of large negative pressure must develop on the downstream side of a closed body for $N \gg 1$. This incompatibility is easily shown by letting $p_1 = -P_o$ ($P_o > 0$) and $u_1 = v_1 = 0$ at some stagnation point x_1, r_1 . Then from eqn. (4.9), which is valid only for inviscid flows, we get

$$\frac{1}{2}(u^2 + v^2) + p < -P_o$$

at any point along the streamline originating from the upstream point x_1, r_1 . Thus, if we require that $p, v \rightarrow 0$ as $x \rightarrow \infty$, this inequality is violated and we must conclude that negative pressures are not allowable at stagnation points in strictly inviscid flows. However, this is not true if viscosity is introduced into the problem because then the pressure can recover to the zero downstream value through the momentum transferred from the outer flow. This is the mechanism proposed by Yonas to explain the results of his experiments but due to the complexity of the problem he was unable to give any details.

In the case of semi-infinite bodies, on the other hand, such stagnant regions of negative pressure are quite unlikely to develop since the flow does not have to close behind the body. In fact, this is supported by some stagnation pressure measurements we made on the Rankine and ogive halfbodies using the drag balance as a pressure transducer. The measured pressures even at the strongest fields were found to be at most 2 to 3 percent higher than the measured pressure without field. Stagnation pressure increases of this order were expected due to a slight pressure drop downstream caused by the

presence of the tow tank walls (see appendix C), but if there had been a more significant pressure drop downstream, it would have acted on the lower bellows of the balance (see figure 3) and produced a corresponding increase in the measured pressure. Thus, it appears that assumption (2) is a reasonable one for semi-infinite bodies. One consequence of this assumption is that it requires the drag of a half-body to be due entirely to excess pressure acting on the nose of the body since the pressure at the base is assumed to be zero.

We must finally consider the third assumption. In order to examine this assumption, Childress (Ref. 34) has suggested describing the flow near infinity and outside the vortical wake by the linearized MFD equations of the Oseen type; i. e., by replacing $(\underline{q}^* \cdot \nabla)$ and $(\underline{B}^* \cdot \nabla)$ with $U \partial / \partial x^*$ and $B_0 \partial / \partial x^*$, respectively. In this approximation, the body is replaced by a concentrated point force at the origin. Solutions to this problem have been carried out by Gourdine (Ref. 6) for arbitrary R_m , Re and N . The most striking feature of these solutions is the appearance of the so-called upstream wake for $\alpha^2 > 1$. Within this wake, the rotational perturbation components ("transverse components") of the axial velocity and magnetic field, denoted as u_x^T and h_x^T by Gourdine, decay algebraically as $x \rightarrow -\infty$. At first glance, one might think by analogy with the viscous Oseen wake that a finite flux of momentum is carried out to upstream infinity in such a wake. However, it can be shown from the results of Gourdine's work that this flux is identically zero for $Re \rightarrow \infty$. The reason for this is that the flux at $x = -\infty$ is given by the sum of an integral of u_x^T and

an integral of h_x^T , and these integrals cancel each other exactly. In fact, for $Re \rightarrow \infty$ it can be easily shown from the x-component of the linearized momentum equations that $p + u' = 0$ (where p and u' are perturbation quantities), from which it is immediately obvious that the total momentum flux of the flow perturbations is zero through any infinite plane located at $x < 0$. The same conclusion holds for the energy flux of the flow perturbations. Thus, these results indicate that assumption (3) may be valid in general.

One final point we should note about the linear solution is that the drag is carried entirely by the downstream viscous wake. For $Re \rightarrow \infty$, this wake degenerates to a singularity along the x-axis given by $u = -H(x) \delta(r)$, where $H(x)$ is the Heaviside function and $\delta(r)$ is the delta function. In a sense, this degenerate wake could be thought of as the representation of the vortical wake in the linear approximation. In fact, Childress (Ref. 34) has attempted to construct a uniformly valid approximation of the flow field by matching the vortical wake to the linear solution. However, the details of his matching procedure are rather obscure to the present author.

This completes our examination of the major assumptions invoked in arriving at eqns. (4.11) and (4.12) and we have at least provided some justification for their validity. However, as useful as these general results have been for qualitative explanations, they still cannot provide us with explicit values of the drag coefficient for $N = O(1)$. This requires solving eqns. (4.1) for $N = O(1)$, but the difficulty is that these equations can no longer be linearized since all terms become of the same order. We can presently only say that

the features of the flow past the streamlined halfbodies at $N = O(1)$ should be qualitatively similar to those at $N \ll 1$ with one important exception. In the former case, a nondiffusive, vortical wake may exist far downstream which could account for a large part of the drag.

4.2 Strong Interaction Case, $N \gg 1$

We shall show that eqns. (4.1) are also basically nonlinear in this case so that solutions were again not obtainable. However, we will still be able to obtain a fairly complete qualitative picture of the flow by making use of some of the general results obtained in the previous section and by examining eqns. (4.1) for $N \gg 1$. Furthermore, we shall obtain a limiting value for the drag coefficient in the limit as $N \rightarrow \infty$.

Any theoretical model of the flow must, of course, be capable of describing the experimental results presented in Sec. 3.1. For large values of N , the main result was that the drag coefficients of all three halfbodies were of $O(1)$ and appeared to be converging to some common value. Before describing our nonlinear theoretical model, it is of interest to compare this empirical result with the results of two existing linear theories.

The first is a theory proposed by Stewartson (Ref. 2) for the limit: $Re \rightarrow \infty$, $Rm \rightarrow 0$ and $\alpha^2 \rightarrow \infty$. He solved a linearized time-dependent problem in this limit for the flow past an infinitely conducting sphere. The same problem was later treated by Ludford and Singh (Ref. 35) who corrected an error made by Stewartson in a boundary condition. However, this resulted in only a slight modification of his solution. They also carried out the solution for the case of the insulated sphere. Both of these solutions gave essentially the same results. In the ultimate steady flow, infinitely-long cylinders of fluid were found both ahead of and behind the sphere and moved with the sphere as if solid. The pressure and radial velocity

both inside and outside these cylinders were found to decay ultimately to zero. The main consequence of this flow model is that the drag is zero.

Now there seems to be no reason why this theory should not give the same solution for a semi-infinite body. In fact, the infinitely-long cylinder of fluid behind the sphere could just as easily be thought of as a solid infinitely-long afterbody. The drag in this case would also be zero. Such a result is obviously in contradiction to the experimental result, and we must therefore reject this theoretical model as physically untrue. The failure of this theory is undoubtedly due to the fact that the nonlinear convection terms were neglected in the equations of motion. Without these terms, excess pressure can never be developed on the nose of the body.

The other linear theory is that of Lary (Ref. 36) who considered inviscid MFD flows past slender bodies. He used the inviscid version of the linear Oseen-type equations solved by Gourdine (c. f., previous section). His results showed that $C_D = O(\epsilon^2 \sqrt{N})$ for $N \gg 1$ where $\epsilon \ll 1$ is the thickness ratio of the body. However, these results are of limited interest to us because the restriction on N for the validity of his theory is $N \ll 1/\epsilon^2$, which means that $C_D < O(\epsilon)$. Therefore, his theory cannot be used to predict C_D of $O(1)$.

In constructing our theoretical model of the flow, we shall first show that the experimental result necessarily implies that stagnant regions of excess pressure must develop in front of the halfbodies. This is easily shown from eqn. (4.10) which, by noting that $C_p = 2p$,

can be put into the form:

$$C_p < 1 - (u^2 + v^2)$$

Since $C_D = 0(1)$, we must have $C_p = 0(1)$ on the front of the halfbodies⁹, which means that $u^2 + v^2 \ll 1$, i. e., the flow is stagnant. We also note from this equation that C_p can never exceed 1. In fact, the maximum pressure is reached at the stagnation point where $C_p = 1$. This follows from eqn. (4.9) since along the dividing streamline, $j^2 = 0$ and so $\underline{q} \cdot \nabla H = 0$.

Given the existence of a stagnant region of excess pressure ahead of the halfbodies, we now ask how this pressure is built up. More specifically, for fixed $x < 0$, how does the pressure rise from its zero freestream value¹⁰ at $r = \infty$ to a value of $0(1)$ as $r \rightarrow 0$? Some idea of how this happens may be obtained by examining eqn. (4.1c), the radial component of the momentum equation. For $N \gg 1$, the inertia terms in this equation may be neglected and we get

$$\frac{\partial p}{\partial r} = -Nv \quad (4.14)$$

Hence, we see that the pressure increase is mainly due to the action of the magnetic force, which in turn depends on the distribution of currents since $j = v$. However, we also wish to know just how the

⁹ This conclusion follows since it was shown in the previous section that the drag of a halfbody is entirely due to excess pressure acting on the front of the body.

¹⁰ In keeping with the definition of the dimensionless pressure given in chapter I, pressures will often be referred to as zero if they equal the freestream pressure p^*_{∞} .

currents are distributed. In an attempt to determine this, we shall first look for a solution of eqns. (4.1) in the limit as $N \rightarrow \infty$. Our procedure will be very similar to that used by Chang (Ref. 37) in his demonstration of the singular perturbation method on another MFD flow problem for the limiting case: $Ha \rightarrow \infty$, $Ha/Re \rightarrow 0$.

We proceed formally by letting $N \rightarrow \infty$ in eqns. (4.1) and keeping (x, r) fixed. The equations which result are

$$v = 0, \quad \frac{\partial u}{\partial x} = 0, \quad \frac{\partial p}{\partial x} = 0$$

The general solution of these equations are

$$v = 0, \quad u = f(r), \quad p = g(r) \quad (4.15)$$

where f and g are arbitrary functions. Now the boundary conditions which must be satisfied are

$$\begin{aligned} \underline{q} \rightarrow \underline{i}, \quad p \rightarrow 0 \quad \text{as} \quad x \rightarrow -\infty, \quad \text{or} \quad r \rightarrow \infty \\ \underline{q} \rightarrow \underline{i} - F(r)\underline{i}, \quad p \rightarrow 0 \quad \text{as} \quad x \rightarrow +\infty \\ \underline{q} \cdot \underline{n} = 0 \quad \text{on the body, } \underline{n} = \text{outward normal to body surface} \end{aligned} \quad (4.16)$$

where $F(r)$ is the unknown wake function defined in the previous section. The development of the downstream vortical wake for the condition, $N \gg 1$, will be discussed later. It is obvious that (4.15) cannot satisfy all of these boundary conditions, which means that the present limit is not uniformly valid and indicates that the problem is of the singular perturbation type (Ref. 38). In anticipation of this, we choose f and g such that (see figure 19)

$$\begin{aligned}
 \underline{q} &= 0, \quad p = \frac{1}{2} && \text{for } r < \frac{1}{2}, \quad x < 0 \\
 \underline{q} &= \underline{i}, \quad p = 0 && \text{for } r > \frac{1}{2}, \quad x < 0 \\
 \underline{q} &= \underline{i} - F \underline{i}, \quad p = 0 && \text{for } r > \frac{1}{2}, \quad x > 0
 \end{aligned} \tag{4.17}$$

Notice that this solution satisfies our requirement for a stagnant region of excess pressure ahead of the body. In fact, we have set the pressure just equal to the maximum pressure of $\frac{1}{2}$ ($C_p = 1$) so this solution must represent the case of maximum drag for which $C_D = 1$. One should also notice that the solution satisfies the boundary conditions on the body, at $r \rightarrow \infty$ and at $x \rightarrow +\infty$. However, it does not satisfy the upstream boundary conditions with $r < \frac{1}{2}$, and it is discontinuous at $r = \frac{1}{2}$ ($x < 0$) and at $x = 0$ ($r > \frac{1}{2}$). In order to satisfy the upstream boundary conditions, an intermediate region (or regions) of flow are required. Intermediate regions are also required at the surfaces on which the discontinuities occur so that a continuous "matching" of the solution can be accomplished (this procedure is well illustrated in reference 37). These intermediate regions of flow will be examined next.

Of particular interest is the pressure jump which occurs across $r = \frac{1}{2}$. This in fact establishes the location of the currents since by eqn. (4.14) such a pressure jump can only occur if there are currents concentrated in a thin layer near $r = \frac{1}{2}$. We can study this current layer in more detail by introducing the scaled variables:

$$x = X(N) \bar{x} = 0(X), \quad r - \frac{1}{2} = \frac{\bar{r}}{R(N)} = 0(1/R) \tag{4.18}$$

and new dependent variables defined by

$$u = \bar{u} = 0(1), v = \frac{\bar{v}}{V(N)} = 0(1/V), p = \bar{p} = 0(1) \quad (4.19)$$

where $R(N)$ and $V(N)$ are undetermined parameters depending on N . In defining the above variables, we have assumed that the current layer thickness is of $0(1/R)$ and that \bar{u} , \bar{v}/V and \bar{p} are the first terms in the expansions of u , v and p in terms of the small parameter $1/N$.

Substitution of (4.18) and (4.19) into eqns. (4.1) gives

$$\frac{1}{X} \frac{\partial \bar{u}}{\partial \bar{x}} + \frac{R}{V} \frac{\partial \bar{v}}{\partial \bar{r}} + \frac{R}{V} \frac{\bar{v}}{\bar{r} - \frac{1}{2}R} = 0 \quad (4.20a)$$

$$\frac{1}{X} \bar{u} \frac{\partial \bar{u}}{\partial \bar{x}} + \bar{v} \frac{\partial \bar{u}}{\partial \bar{r}} = -\frac{1}{X} \frac{\partial \bar{p}}{\partial \bar{x}} \quad (4.20b)$$

$$\frac{1}{XV} \bar{u} \frac{\partial \bar{v}}{\partial \bar{x}} + \frac{R}{V^2} \bar{v} \frac{\partial \bar{v}}{\partial \bar{r}} = -R \frac{\partial \bar{p}}{\partial \bar{r}} - \frac{N}{V} \bar{v} \quad (4.20c)$$

Now the pressure term in eqn. (4.20c) can balance the magnetic term only if $R = N/V$. Also, eqn. (4.20a) can only be satisfied if $1/X = R/V$. Hence, we must have

$$\frac{1}{R} = \sqrt{\frac{X}{N}}, \quad \frac{1}{V} = \frac{1}{\sqrt{NX}} \quad (4.21)$$

Then in the limit as $N \rightarrow \infty$, eqns. (4.20) must reduce to

$$\frac{\partial \bar{u}}{\partial \bar{x}} + \frac{\partial \bar{v}}{\partial \bar{r}} = 0$$

$$\bar{u} \frac{\partial \bar{u}}{\partial \bar{x}} + \bar{v} \frac{\partial \bar{u}}{\partial \bar{r}} = - \frac{\partial \bar{p}}{\partial \bar{x}} \quad (4.22)$$

$$\frac{\partial \bar{p}}{\partial \bar{r}} = - \bar{v}$$

Note that the nonlinear inertia terms survive in the x-component of the momentum equation. These terms are essential in order to balance the large changes in pressure which occur along the stream-wise direction, but they are also the greatest obstacles standing in the way of solutions to eqns. (4.1).

From (4.21) we can now give the following estimates of the current layer thickness, δ , and the magnitude of the currents, $j = v$:

$$\delta = O(1/R) = O(\sqrt{X/N}) = \begin{cases} O(1/\sqrt{N}) & \text{for } X = 1 \\ O(1) & \text{for } X = N \end{cases}$$

$$j = O(1/V) = O(1/\sqrt{NX}) = \begin{cases} O(1/\sqrt{N}) & \text{for } X = 1 \\ O(1/N) & \text{for } X = N \end{cases}$$

Thus, the current layers must spread from a thickness of $O(1/\sqrt{N})$ at $x = O(1)$ and merge into a single layer of thickness $O(1)$ at $x = O(N)$.

The spreading of these layers is illustrated in figure 20.

We can also estimate the current dissipation in the layers as follows:

$$N \int j^2 dV = O(N j^2 X \delta) = O(N \frac{1}{NX} X \sqrt{\frac{X}{N}}) = O(1)$$

Hence, the current dissipation remains finite as $N \rightarrow \infty$ even though $\delta \rightarrow 0$ and $j \rightarrow 0$.

The thin current layer model described above was first mentioned by Childress (Ref. 39) in analogy with a solution he carried out for the case, $N/Re \gg 1$. It was later developed in more detail by Yonas (Ref. 10) who proposed that such current layers could support not only stagnant regions of positive pressure in front of a closed body, but also stagnant regions of negative pressure behind the body.

The merging of the current layers near $x = O(N)$ into a single wake-like region suggests the possibility of matching it to the upstream wake given by Gourdine's linear solution (Ref. 6). This linear solution could then satisfy the upstream boundary conditions. However, such a matching is not possible because the linear solution cannot match pressures of $O(1)$ and still be valid. Therefore, there must be at least one intermediate region between the stagnant region and the region far upstream where the linear solution is valid.

In order to determine the equations for this intermediate region, we introduce the following limit process:

$$x = X(N) \quad \tilde{x} = O(X), \quad r = \tilde{r} = O(1)$$

$$u = \tilde{u} = O(1) \quad , \quad v = \frac{\tilde{v}}{V(N)} = O(1/V) \quad , \quad p = \tilde{p} = O(1)$$

Substituting these variables into eqns. (4.1) and proceeding as before, we find that

$$X = V = N$$

so that

$$j = v = 0(1/N)$$

And in the limit as $N \rightarrow \infty$, eqns. (4.1) reduce to

$$\begin{aligned} \frac{\partial \tilde{u}}{\partial \tilde{x}} + \frac{\partial \tilde{v}}{\partial \tilde{r}} &= 0 \\ \tilde{u} \frac{\partial \tilde{u}}{\partial \tilde{x}} + \tilde{v} \frac{\partial \tilde{u}}{\partial \tilde{r}} &= - \frac{\partial \tilde{p}}{\partial \tilde{x}} \\ \frac{\partial \tilde{p}}{\partial \tilde{r}} &= - \tilde{v} \end{aligned} \tag{4.23}$$

which are identical to eqns. (4.22) for the current layers. Thus, the equations for this intermediate region are also basically nonlinear. However, these equations may be valid over a much wider region. In fact, Childress (Ref. 15) has attempted to apply eqns. (4.23) to the entire flow field in order to determine the drag of a two-dimensional circular cylinder. In the strained coordinate system of these equations, such a cylinder simply appears as a flat plate on which simpler boundary conditions may be specified. Using a successive approximations technique to solve eqns. (4.23), Childress found $C_D = 0.721$ from the first approximation. Due to the increasing complexity of the equations, he was unable to carry the solution to higher approximations. However, it would seem clear without calculation that higher approximations should lead to $C_D \rightarrow 1$ since Childress assumed $C_p = 0$ on the rear of the plate and we have shown

that $C_p \rightarrow 1$ on the front of a body as $N \rightarrow \infty$. Yonas (Ref. 10) has also alluded to this point.

It should also be mentioned here that an exact similarity solution of eqns. (4.23) has been found by Kovasznay and Fung (Ref. 40) and by Childress (Ref. 34). However, it corresponds to sink flow at high N and finds no application to flow past bodies.

We must finally consider the nonuniformity near $x = 0$ ($r > \frac{1}{2}$). The detailed structure of this region appears to be quite complicated and, in fact, there may be more than one region required in order to describe it. Unlike the previous two regions, a consistent limit process could not be defined which yielded a unique set of equations. The proper equations can probably only be determined by obtaining explicit solutions and carrying out the difficult matching of the various regions which come together at $x = 0$, $r = \frac{1}{2}$. Although we can presently say very little about the detailed structure of the flow in this region, it probably would not add anything essential to our qualitative understanding of the overall flow.

This completes our descriptive analysis of the various regions of nonuniformity, but so far we have said very little about the non-diffusive, vortical wake which has been assumed to exist far downstream. However, it has already been shown that the Joule dissipation in the current layers remains finite as $N \rightarrow \infty$. This implies that there will always be a decrease in the Bernoulli H-function along the streamlines, which in turn means that a vortical wake must exist far downstream. This can also be shown from eqn. (4.12) which gives the drag

coefficient in terms of an integral of the F-function, and is supposedly valid for arbitrary N. We see from this equation that if $C_D \rightarrow 1$ as $N \rightarrow \infty$, then F cannot approach 1, 0 or change abruptly from 0 to 1 anywhere, for otherwise, $C_D \rightarrow 0$.

A possible profile for the F-function is shown in figure 21 where we have also tried to summarize what has been deduced about the structure of the rest of the flow field in the limit $N \rightarrow \infty$. A stagnant region in which $C_p = 1$ extends from the front of the body to $x = -\infty$. The pressure in this region is supported by a cylindrical current sheet at $r = \frac{1}{2}$ in which the currents are becoming vanishingly small. Outside this current sheet at $x \rightarrow \infty$, the velocity is parallel and equal to unity and the pressure is zero. Far downstream, the pressure is again zero and the flow is parallel, but there is a nondiffusive, vortical wake. All these features of the limiting flow field are quite consistent with the trend of the experimental results. Since the body shape is immaterial in this limiting flow field, it explains why the drag coefficient curves of all three halfbodies appear to be converging into one. Furthermore, the drag coefficient of a halfbody in the limiting flow field is unity, and indeed, the drag coefficients of the halfbodies do appear to be gradually approaching this upper limit.

The physical model we have described above has led to considerable insight into the structure of the flow field for $N \gg 1$. Although the model is admittedly incomplete in many of its details and we are unable to provide explicit calculations of the drag for large, finite values of N, most of the fundamental features of the flow appear to be qualitatively well-understood.

V. CONCLUSION

Results have been presented from MFD drag measurements on three semi-infinite bodies over the range, $0 \leq N \leq 24$. Two of the bodies, a Rankine halfbody and a 2-caliber ogive, were streamlined shapes, and the third was a blunt halfbody. For $N \leq 0(1)$, the drag coefficients of the streamlined halfbodies were found to increase linearly with N , but the drag coefficient of the blunt halfbody was relatively unaffected. For $N \gg 1$, the drag coefficients of all three halfbodies were of $O(1)$ and appeared to be asymptotically converging to some common limiting value.

A simple theoretical calculation of the drag coefficient of the Rankine halfbody was possible for $N \ll 1$ which agreed quite well with the experimental results. However, there was apparent agreement even for $N = O(1)$ for which the theoretical calculation is no longer valid. This was explained by a strictly inviscid theory which showed that a nondiffusive, vortical wake must exist at downstream infinity. By extending the results of this inviscid theory to the case $N \gg 1$, a physical model of the flow was constructed which led to the conclusion that as $N \rightarrow \infty$ an infinitely-long stagnant slug must form in front of a halfbody and the drag coefficient of the body must approach a maximum value of unity. Although all the features of this model are consistent with the trend of the experimental results, more complete experimental verification is needed.

It is particularly important to establish the extent to which the inviscid flow approximation is valid. This might be studied by

measuring the wake velocities at various distances downstream. Also in question is the existence of the thin current layers and long stagnant slugs in front of the halfbodies. The answer to this question could be provided by detailed measurements of the velocity and magnetic field.

There is perhaps even a greater need for further theoretical work on the problem. Although the MFD drag can be calculated for small N and an upper bound on its value has been established for $N \rightarrow \infty$, it cannot as yet be calculated for intermediate values of N . Hopefully, the physical framework that has been provided here will prove beneficial in this endeavor.

Finally, results have also been presented from measurements made of the transient drag of flat disks which were started impulsively from rest. The drag of a disk was found to overshoot its steady-state value by 30 to 50 per cent and required a distance of about 25 disk diameters to reach this steady-state value. This behavior was attributed to the vortex formation process occurring in the wake of the disk. Additional experiments, particularly visual flow studies, would probably lead to a better understanding of this interesting process.

REFERENCES

1. Liepmann, H. W. , Hoult, D. P. , and Ahlstrom, H. G. , "Concept, Construction, and Preliminary Use of a Facility for Experimental Studies in Magneto-Fluid Dynamics," Miszellen der Angewandten Mechanick, 175-189, 1960.
2. Stewartson, K. , "Motion of a Sphere Through a Conducting Fluid in the Presence of a Strong Magnetic Field," Proc. Camb. Phil. Soc. 52, 301-316 (1956).
3. Chester, W. , "The Effect of a Magnetic Field on Stokes Flow in a Conducting Fluid," J. Fluid Mech. 3, 304-308 (1957).
4. Sears, W. R. and Resler, E. L. Jr. , "Theory of Thin Airfoils in Fluids of High Electrical Conductivity," J. Fluid Mech. 5, 257-273 (1959).
5. Stewartson, K. , "On the Motion of a Non-Conducting Body Through a Perfectly Conducting Fluid," J. Fluid Mech. 8, 82-96 (1960).
6. Gourdine, M. C. , "On Magnetohydrodynamic Flow over Solids," Ph.D. Thesis, California Institute of Technology, 1960. Also see: J. Fluid Mech. 10, 459-465 (1961).
7. Maxworthy, T. , "Measurements of Drag and Wake Structure in Magneto-Fluid Dynamic Flow about a Sphere," Heat Transfer and Fluid Mech. Inst. , 197-205, 1962.
8. Ahlstrom, H. G. , "Experiments on the Upstream Wake in Magneto-Fluid Dynamics," J. Fluid Mech. 15, 205-221 (1963).
9. Motz, R. O. , "Magnetohydrodynamic Drag on a Oscillating Sphere," J. Fluid Mech. 24, 705-720 (1966).

10. Yonas, G. , "Aligned Fields, Magneto-Fluid Dynamic Flow Past Bodies," Ph. D. Thesis, California Institute of Technology, 1966.
11. Dorman, L. I. and Mikhailov, Y. M. , "Investigation of Electro-Magnetic Phenomena Involved in the Motion of Bodies in a Conducting Fluid in a Magnetic Field," Sov. Phys. JETP 16, 531 (1963).
12. Shercliff, J. A. , A Textbook of Magnetohydrodynamics, Permagon, 1965.
13. Chester, W. , "The Effect of a Magnetic Field on the Flow of a Conducting Fluid Past a Body of Revolution," J. Fluid Mech. 10, 459-465 (1961).
14. Hoerner, Fluid-Dynamic Drag; Practical Information on Aerodynamic Drag and Hydrodynamic Resistance, Midland Park, 1965.
15. Childress, S. , "Inviscid Magnetohydrodynamic Flow in the Presence of a Strong Magnetic Field," JPL SPS No. 37-22, 254-255 (1963).
16. Goldstein, S. , Modern Developments in Fluid Dynamics, Vol. II, Clarendon, 1938.
17. Rouse, H. and Howe, J. W. , Basic Mechanics of Fluids, Wiley and Sons, 1953.
18. Schmidt, F. S. , "Zur beschleunigten Bewegung kugelförmiger Körper in widerstehenden Mitteln," Diss. , Leipzig, 1919.

19. Schwabe, M. , "Pressure Distribution in Nonuniform Two-Dimensional Flow," NACA TM No. 1039, Jan. 1943.
Translated from: Ingenieur-Archiv, Vol. VI (Feb. 1939).
20. Sarpkaya, T. , "Separated Flow about Lifting Bodies and Impulsive Flow about Cylinders," AIAA Journ. 4, 414-420, (1966).
21. Kendall, J. M. , Jr. , "The Periodic Wake of a Sphere," JPL SPS No. 37-25 (1964).
22. Fromm, J. E. and Harlow, F. H. , "Numerical Solution of the Problem of Vortex Street Development," Phys. Fluids 6, 975-982 (1963).
23. International Critical Tables of Numerical Data, Physics, Chemistry and Technology, McGraw-Hill, 1929.
24. Maxworthy, T. , private communication.
25. Lake, B. M. , private communication.
26. Liepmann, H. W. , "Hydromagnetic Effects in Couette and Stokes Flow," The Plasma in a Magnetic Field; A Symposium on Magnetohydrodynamics, (ed. , Landshoff, R. K. M.), 117-130, 1958.
27. Chopra, K. P. and Singer, S. F. , "Drag of a Sphere Moving in a Conducting Fluid in the Presence of a Magnetic Field," Heat Transfer and Fluid Mech. Inst. , 166-175, 1958.
28. Reitz, J. R. and Foldy, L. L. , "The Force on a Sphere Moving Through a Conducting Fluid in the Presence of a Magnetic Field," J. Fluid Mech. 11, 133-142 (1961).

29. Ludford, G. S. S. , "Inviscid Flow Past a Body at Low Magnetic Reynolds Number," Rev. Mod. Phys. 32, 1000-1003 (1960).
30. Ludford, G. S. S. and Murray, J. D. , "On the Flow of a Conducting Fluid Past a Magnetized Sphere," J. of Fluid Mech. 7, 516-528 (1960).
31. Milne-Thompson, L. M. , Theoretical Hydrodynamics, Macmillan, 1950.
32. Tamada, K. , "Flow of a Slightly Conducting Fluid Past a Circular Cylinder with Strong, Aligned Field," Phys. of Fluids 5, 817-823 (1962).
33. Leonard, B. , "Some Aspects of Magnetohydrodynamic Flow about a Blunt Body," AFOSR 2714, 1962.
34. Childress, S. , "On the Flow of a Conducting Fluid of Small Viscosity," JPL Tech. Rept. No. 32-351, Jan. 1963.
35. Ludford, G. S. S. and Singh, M. P. "On the Motion of a Sphere Through a Conducting Fluid in the Presence of a Magnetic Field," Proc. Camb. Phil. Soc. 59, 625-635 (1963).
36. Lary, E. C. , "A Theory of Thin Airfoils and Slender Bodies in Fluids of Finite Electrical Conductivity with Aligned Fields," J. Fluid Mech. 12, 209-226 (1962).
37. Chang, I. D. , "On a Singular Perturbation Problem in Magnetohydrodynamics," Zeits. f. angew. Math. und Phys. 14, 134-147 (1963).
38. Cole, J. D. , Perturbation Methods in Applied Mathematics, Blaisdell, (to be published).

39. Childress, S. , "The Effect of a Strong Magnetic Field on Two-Dimensional Flows of a Conducting Fluid," J. Fluid Mech. 15, 429-441 (1963).
40. Kovaszny, L. S. G. and Fung, F. C. W. , "Asymptotic Solutions for Sink Flow in a Strong Magnetic Field," Phys. of Fluids 5, 661-664 (1962).
41. Schlichting, H. , Boundary Layer Theory, McGraw-Hill, 1960.
42. Greenspan, H. P. and Carrier, G. F. , "The Magnetohydrodynamic Flow Past a Flat Plate," J. Fluid Mech. 6, 77-96 (1959).
43. Stewartson, K. , "On Magnetic Boundary Layers," J. Inst. Math. Applic. 1, 29-41 (1965).

APPENDICES

A. Calculation of Base Drag without Dissipation

The base drag will be calculated assuming that the flow is inviscid and non-dissipative. The coordinate frame is fixed to the halfbody and a control volume is selected which consists of the tow tank walls and two cross-sections, I and II, of the tow tank as shown in figure 10. The entry cross-section I of area A_1 is chosen far enough upstream such that the velocity u_1 and pressure p_1 are uniform across it. Likewise, the exit cross-section II of area A_2 is chosen far enough downstream such that the velocity u_2 and pressure p_2 are uniform across it. These latter conditions are assumed to exist by the time the flow reaches the lower bellows of the drag balance. Under the above assumptions, the conservation equations may be written as follows:

$$u_1 A_1 = u_2 A_2 \quad (\text{Continuity})$$

$$p_1 A_1 + \rho u_1^2 A_1 = p_2 A_2 + \rho u_2^2 A_2 + D \quad (\text{Momentum})$$

$$p_1 u_1 A_1 + \frac{1}{2} \rho u_1^3 A_1 = p_2 u_2 A_2 + \frac{1}{2} \rho u_2^3 A_2 \quad (\text{Energy, or Bernoulli law})$$

Elimination of u_2 and p_2 from these equations leads to

$$D + p_1(A_1 - A_2) = \frac{1}{2} \rho u_1^2 \frac{A_1}{A_2} \left(1 - \frac{A_1}{A_2}\right)$$

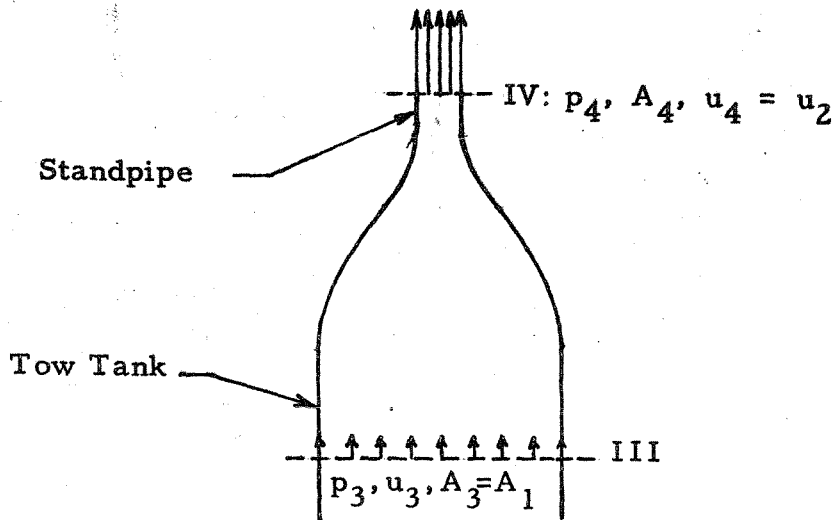
Since the drag is always measured with reference to p_1 , we can simply set $p_1 = 0$. The drag coefficient is then given by

$$C_D = \frac{D}{\frac{1}{2} \rho u_1^2 (A_1 - A_2)} = \frac{A_1}{A_2} \left(\frac{A_1}{A_2} - 1 \right)$$

Since $A_1/A_2 = 1.035$ for the tow tank, $C_D = 0.0357$.

B. Calculation of Pressure Jump due to Flow in Standpipe

The pressure jump in the tow tank due to the acceleration of the mercury flowing into the standpipe may be easily calculated by considering the balance of mass and energy of the system shown in the sketch below:



Again, the flow is assumed to be inviscid and the velocities and pressures at sections III and IV are assumed uniform. The velocity u_3 is just the velocity of the fluid displaced by the drive shaft, and since the ID of the standpipe equals the OD of the drive shaft, u_4 is just equal to the drive shaft velocity, u_2 . Conservation of mass and energy then gives:

$$u_3 A_3 = u_4 A_4, \quad \text{where } u_4 = u_2 \text{ and } A_3 = A_1$$

$$\frac{1}{2} \rho u_3^3 A_3 + p_3 u_3 A_3 = \frac{1}{2} \rho u_4^3 A_4 + p_4 u_4 A_4$$

A little algebra then gives the pressure jump as

$$\frac{p_3 - p_4}{\frac{1}{2} \rho u_2^2} = \left(1 - \frac{u_3^2}{u_2^2}\right) = \left(1 - \frac{A_4^2}{A_1^2}\right) \approx 1$$

since $A_4/A_1 \approx 1/30$.

Now if the difference in the effective areas of the bellows is ΔA_b and the cross-sectional area of a model is A , then the drag coefficient corresponding to the apparent drag force produced by the pressure jump is

$$C_D = \frac{(p_3 - p_4) \Delta A_b}{\frac{1}{2} \rho u_1^2 A} \approx \frac{p_3 - p_4}{\frac{1}{2} \rho u_2^2} \cdot \frac{A_b}{A} \cdot \frac{\Delta A_b}{A_b} \approx 1 \frac{\Delta A_b/A_b}{A/A_b}$$

The ratio A/A_b , where A_b is the average effective area of the bellows, is 5.5 and $\Delta A_b/A_b$ is about .025 (this was determined by increasing the mercury hydrostatic head by a known amount and measuring the change in the drag balance output). Therefore, $C_D \approx .025/5.5 \approx .004$.

It should also be noted that there may be an additional pressure increase in the tow tank due to viscous effects in the standpipe flow.

However, this increase was calculated assuming fully-developed

turbulent flow and was found to be only about 10 percent of the pressure jump calculated above.

C. Calculation of Base Drag with Dissipation

We again choose the control volume shown in figure 10. As in the non-dissipative case (appendix A), the conditions across section I are assumed to be uniform. However, we can no longer make this assumption about the conditions across section II. If kinetic energy is being dissipated in the region near the nose, due either to viscous or ohmic losses, then a vortical wake forms downstream and the velocity across section II may appear as shown by the dashed line denoted as \tilde{u}_2 in figure 10. In any real flow, this wake is ultimately dissipated very far downstream by the action of viscosity and uniform flow conditions are regained.

Although the velocity \tilde{u}_2 is nonuniform across section II, if this section is taken sufficiently far downstream (say at the location of the lower bellows), then the streamlines should become nearly parallel and the pressure across the section may be assumed constant. Under this assumption, the continuity and energy equations for the system may be written as follows:

$$u_1 A_1 = \int_{A_2} \tilde{u}_2 dA_2 = u_2 A_2 \quad (C.1)$$

$$Q_1 = \frac{1}{2} \rho u_1^3 A_1 - \frac{1}{2} \rho \int_{A_2} \tilde{u}_2^3 dA_2 + p_1 u_1 A_1 - p_2 \int_{A_2} \tilde{u}_2 dA_2 \quad (C.2)$$

where Q_1 is the dissipation per unit time within the control volume.

Using (C. 1) in (C. 2), we get

$$(p_2 - p_1) u_1 A_1 = -Q_1 + \frac{1}{2} \rho u_1^3 A_1 - \frac{1}{2} \rho \int_{A_2} \tilde{u}_2^3 dA_2$$

Or

$$C_{P_2} = \frac{p_2 - p_1}{\frac{1}{2} \rho u_1^2} = -\frac{Q_1}{\frac{1}{2} \rho u_1^3 A_1} + 1 - \frac{A_1^2}{A_2^2} \left[\frac{1}{A_2 u_2^3} \int_{A_2} \tilde{u}_2^3 dA_2 \right] \quad (C. 3)$$

It will be shown below that the term in brackets may differ from unity by only 1 per cent so that it will simply be taken equal to unity. We estimate Q_1 by noting that the work done by the drag force, Du_2 , is not only dissipated into heat but an appreciable fraction may also be carried out of the control volume as kinetic energy by the vortical wake. This is shown explicitly in Sec. 4.1 for the case illustrated in figure 18a. Thus, if we let $Q_1 = \beta Du_2$ ($0 < \beta < 1$), then (C. 3) can be written as

$$\begin{aligned} C_{P_2} &= -\beta \frac{D}{\frac{1}{2} \rho u_1^2 u_1 A_1} \frac{u_2}{u_1} - \left(1 - \frac{A_1^2}{A_2^2} \right) \\ &= -\beta C_D \frac{A_1 - A_2}{A_2} - \left(1 - \frac{A_1^2}{A_2^2} \right) \end{aligned}$$

where

$$C_D = \frac{D}{\frac{1}{2} \rho u_1^2 (A_1 - A_2)}$$

For the tow tank, $A_1/A_2 = 1.035$ so

$$C_{P_2} = -.035 \beta C_D - .070 \quad (C. 4)$$

This result is essentially a statement of the simple fact that the pressure in a pipe should drop if there is any dissipation. Without dissipation the pressure drop is given by $C_{P_2} = -.070$, so that the term $-.035 \beta C_D$ is a measure of the pressure drop due to dissipation.

We shall now go back and estimate the term in brackets in eqn. (C. 3) which was taken to be unity in arriving at eqn. (C. 4). This term will be estimated by considering the fictitious process in which the vortical wake, \tilde{u}_2 , flowing out of section II is ultimately dissipated as heat, Q_2 , such that the velocity becomes uniform again across some section III farther downstream¹. The mass and energy balances for the fluid between sections II and III give

$$\int_{A_2} \tilde{u}_2 \, dA_2 = u_2 A_2 = u_3 A_3$$

and

$$Q_2 = \frac{1}{2} \rho \int_{A_2} \tilde{u}_2^3 \, dA_2 + p_2 u_2 A_2 - \frac{1}{2} \rho u_3^3 A_3 - p_3 u_3 A_3$$

¹ The process is fictitious because in the real flow the effects of the halfbody boundary layer are bound to become important very far downstream and the flow will approach cylindrical Couette flow. However, by considering such a fictitious process, we can ignore these effects.

Since $A_3 = A_2$, $u_3 = u_2$ and the energy equation may be rewritten as

$$\frac{1}{2}\rho \int_{A_2} \tilde{u}_2^3 dA_2 = \frac{1}{2}\rho u_2^3 A_2 + Q_2 - (p_2 - p_3)u_2 A_2$$

But $p_2 - p_3 > 0$, so

$$\frac{1}{2}\rho \int_{A_2} \tilde{u}_2^3 dA_2 < \frac{1}{2}\rho u_2^3 A_2 + Q_2$$

Or

$$\left[\frac{1}{A_2 u_2^3} \int_{A_2} \tilde{u}_2^3 dA_2 \right] < 1 + \frac{Q_2}{\frac{1}{2}\rho u_2^3 A_2}$$

By the same argument used above for Q_1 , we can set $Q_2 = \gamma Du_2$, $0 < \gamma < 1$.

In particular, we assume $\gamma = \frac{1}{2}$ which is probably as good a guess as any. Then the above relation becomes

$$\left[\frac{1}{A_2 u_2^3} \int_{A_2} \tilde{u}_2^3 dA_2 \right] < 1 + \frac{1}{2} \frac{A_2}{A_1} \cdot \frac{A_1 - A_2}{A_1} C_D = 1.015 \text{ for } C_D = 1$$

which gives the required result.

From eqn. (C.4) we can now obtain an estimate for C_{p_2} . For the blunt halfbody we take $C_D = .8$ and rather arbitrarily assume $\beta = \frac{1}{2}$.

The pressure drop is then given by

$$C_{p_2} \approx -.08$$

This admittedly crude estimate is probably as good (or bad) for $N = 0$ as it is for $N > 0$ since C_D does not vary much with N (c. f. , Sec. 3. 1) and the dissipation within the control volume probably stays about the same even though the dominant dissipative mechanism may change from viscous to ohmic. In any case, the estimate cannot be too far off since for $C_D = 1$ and $\beta = 1$, (C. 4) gives

$$C_{P_2} = - .105 \quad (C. 5)$$

In the case of the Rankine and ogive halfbodies, the dissipation was almost zero at $N = 0$, but surely increased as N increased², corresponding to an increase in βC_D in eqn. (C. 4). Thus, C_{P_2} must have decreased accordingly as N increased. However, it is shown in Sec. 4. 2 that $C_D \leq 1$, so that C_{P_2} cannot decrease below the value given by (C. 5)³, which corresponds to a maximum base drag coefficient of $C_{D_b} = +.105$. Therefore, the base drag coefficients of the Rankine and ogive halfbodies must vary from their zero-field value of .036 (c. f. appendix A) to a maximum value of .105 as N becomes very large.

D. Derivation of MFD Boundary Layer Equations

We consider the laminar flow of a conducting fluid past an insulated flat plate for the following conditions:

$$Rm \ll 1, N \gg 1, Re \gg 1 \text{ and } N/Re \ll 1 \quad (D. 1)$$

² In Sec. 3. 1 it will be shown that C_D increases monotonically with N .

³ Some stagnation pressure measurements described in Sec. 4. 1 (pp. 54 -55) indicate that the pressure at the lower bellows of the drag balance does not in fact decrease below this value.

We shall assume that $Re \rightarrow 0$ so that eqns. (1.1a) and (1.1b) can be used with $\underline{B} = -\underline{i}$. The variables are then defined as follows:

$$\begin{aligned} u &= \bar{u} = 0(1) \quad , \quad v = V(Re, N)\bar{v} = 0(V) \quad , \quad p = P(Re, N)\bar{p} = 0(P) \\ x &= \bar{x} = 0(1) \quad , \quad y = Y(Re, N)\bar{y} = 0(Y) \end{aligned} \quad (D. 2)$$

where V , P and Y are unknown scaling factors which depend on Re and N . Since we want to relate the results of this analysis to the boundary layer flow over a halfbody, it was convenient to retain the halfbody diameter, d , as the characteristic length in defining the parameters in (D.1) and the dimensionless variables, x and y , in (D.2). Note that this implies $x^* = xd = 0(d)$. In terms of the variables defined in (D.2), the continuity and momentum equations take the following forms:

$$\frac{\partial \bar{u}}{\partial \bar{x}} + \frac{V}{Y} \frac{\partial \bar{v}}{\partial \bar{y}} = 0 \quad (D. 3a)$$

$$\bar{u} \frac{\partial \bar{u}}{\partial \bar{x}} + \frac{V}{Y} \bar{v} \frac{\partial \bar{u}}{\partial \bar{y}} = -P \frac{\partial \bar{p}}{\partial \bar{x}} + \frac{1}{Re} \left(\frac{\partial^2 \bar{u}}{\partial \bar{x}^2} + \frac{1}{Y^2} \frac{\partial^2 \bar{u}}{\partial \bar{y}^2} \right) \quad (D. 3b)$$

$$V^2 \bar{v} \frac{\partial \bar{v}}{\partial \bar{x}} + \frac{V}{Y} \bar{u} \frac{\partial \bar{v}}{\partial \bar{y}} = -\frac{P}{Y} \frac{\partial \bar{p}}{\partial \bar{y}} - NV \bar{v} + \frac{1}{Re} \left(V \frac{\partial^2 \bar{v}}{\partial \bar{x}^2} + \frac{V}{Y^2} \frac{\partial^2 \bar{v}}{\partial \bar{y}^2} \right) \quad (D. 3c)$$

Now eqn. (D.3a) can only be satisfied if $V = Y$. The viscous and inertia forces in eqn. (D.3b) can then be balanced by requiring that

$$Y = \frac{1}{\sqrt{Re}} = V$$

The only terms that can now be balanced in eqn. (D. 3c) is the pressure gradient against the magnetic force. This requires that

$$P = \frac{N}{Re}$$

Thus, the following estimates have been obtained:

$$v = O(Re^{-\frac{1}{2}}), \quad p = O(N/Re), \quad \delta = O(Re^{-\frac{1}{2}}) \quad (D. 4)$$

where $\delta = \delta^*/d$ is the dimensionless boundary layer thickness. In the limit, $Re \rightarrow \infty$, $N \rightarrow \infty$, eqns. (D. 3) reduce to

$$\frac{\partial \bar{u}}{\partial \bar{x}} + \frac{\partial \bar{v}}{\partial \bar{y}} = 0$$

$$u \frac{\partial \bar{u}}{\partial \bar{x}} + \bar{v} \frac{\partial \bar{u}}{\partial \bar{y}} = \frac{\partial^2 \bar{u}}{\partial \bar{y}^2}$$

$$\frac{\partial \bar{p}}{\partial \bar{y}} = -\bar{v}$$

The first two equations are just the ordinary boundary layer equations for a flat plate. The third equation gives the pressure across the boundary layer once \bar{v} is obtained from the solution of the first two equations. However, the Blasius solution for \bar{v} leads to $\partial \bar{p} / \partial \bar{x} > 0$ so if this term were included in the second equation above, it would cause the flow to decelerate and boundary layer to thicken. Therefore, we must examine this effect more closely in order to determine if it can cause the boundary layer to separate. A crude estimate can be made by evaluating the Kármán-Pohlhausen parameter Λ (Ref. 41):

$$\Lambda = \frac{\delta^{*2}}{\rho \nu U} \frac{dp^*}{dx^*} = \frac{\delta^{*2}}{\rho \nu U} \frac{\rho U^2}{d} \frac{dp}{dx} = \text{Re} \delta^2 \frac{dp}{dx}$$

Now from (D.4)

$$\delta=0(V) = 0(1/\sqrt{\text{Re}}) \quad , \quad \frac{dp}{dx} = 0(P) = 0(N/\text{Re})$$

Hence,

$$\Lambda = 0(N/\text{Re}) \ll 1$$

Since the criterion for separation is $\Lambda = -12$, this estimate indicates that separation is very unlikely.

Thus, we have shown that the ordinary boundary layer equations are very likely to be valid for the conditions given by (D.1). No unusual effects, such as upstream-growing boundary layers and reversed flow (indicating a breakdown in the boundary layer equations) which have been predicted by some theoretical solutions (e.g., Refs. 42 and 43), are expected for these conditions because the interaction between the flow and the magnetic field is extremely weak.

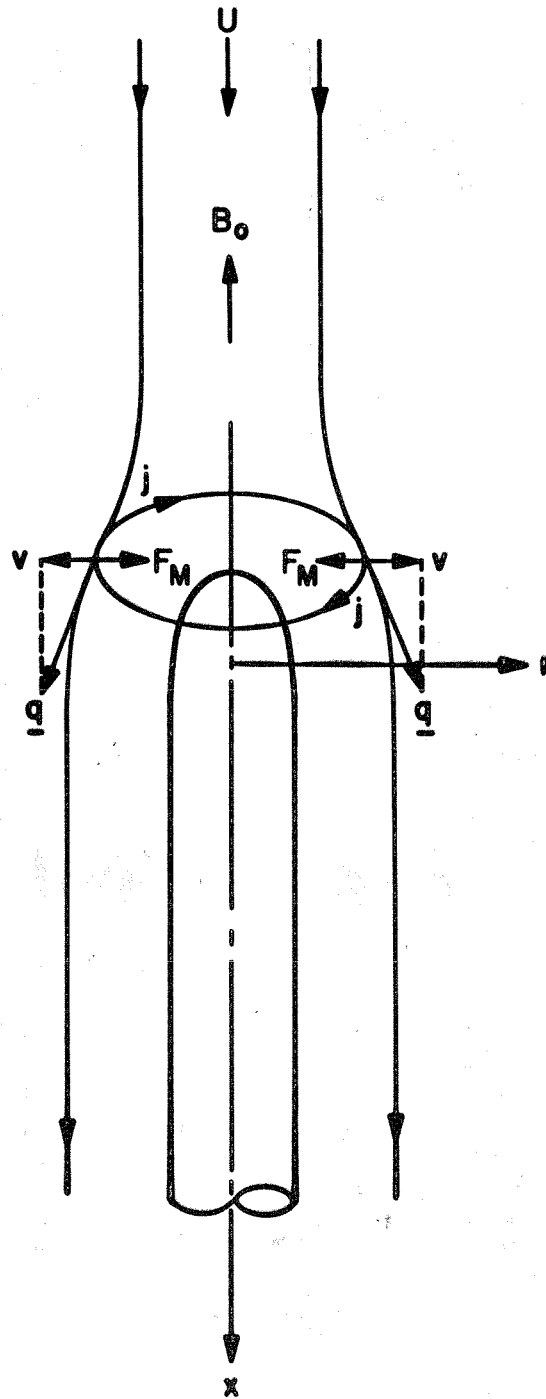


Figure 1. CURRENTS AND MAGNETIC FORCES IN AXI-SYMMETRIC MFD FLOW IN THE LIMIT $Rm \rightarrow 0$

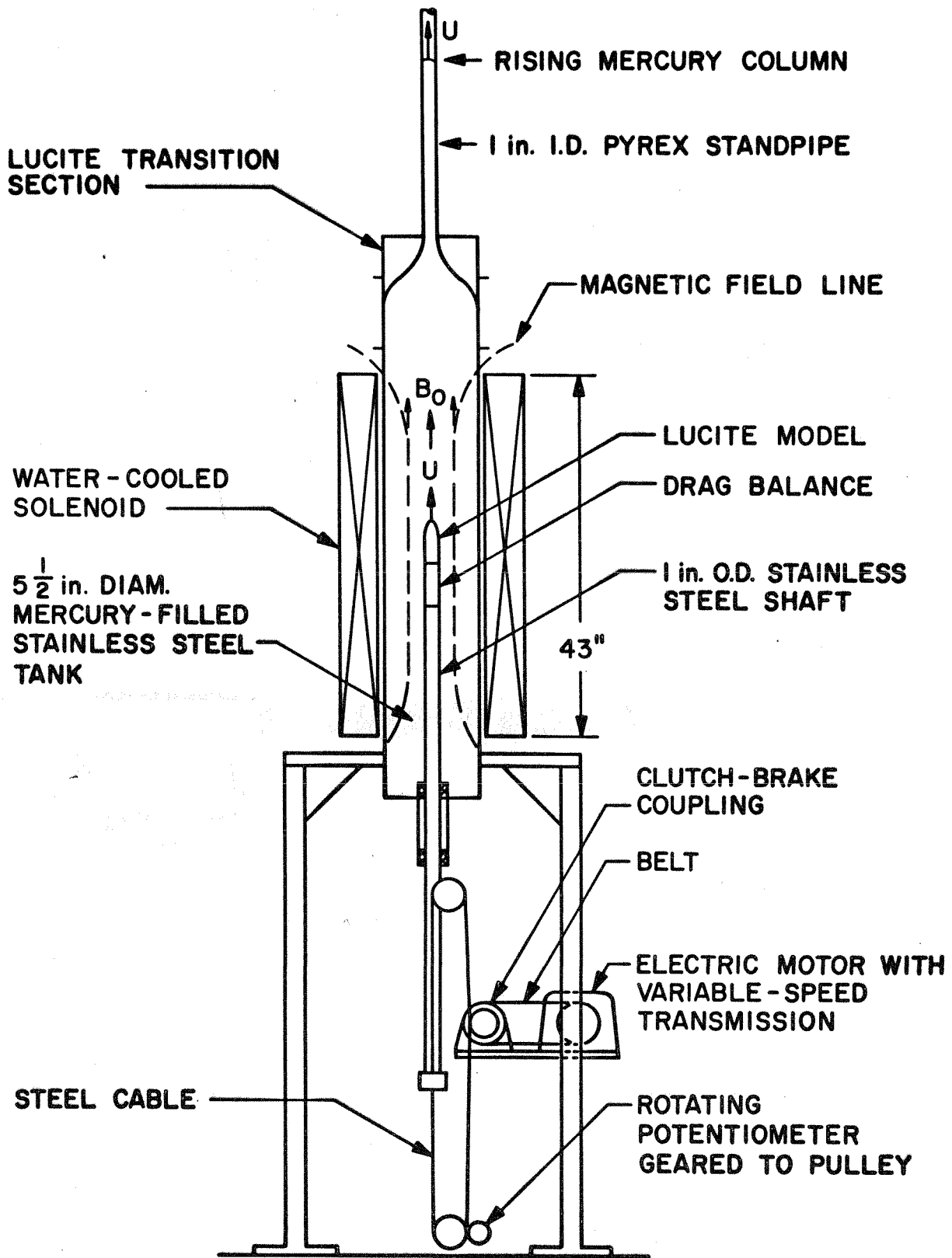


Figure 2. SCHEMATIC DIAGRAM OF THE MERCURY TOW TANK.

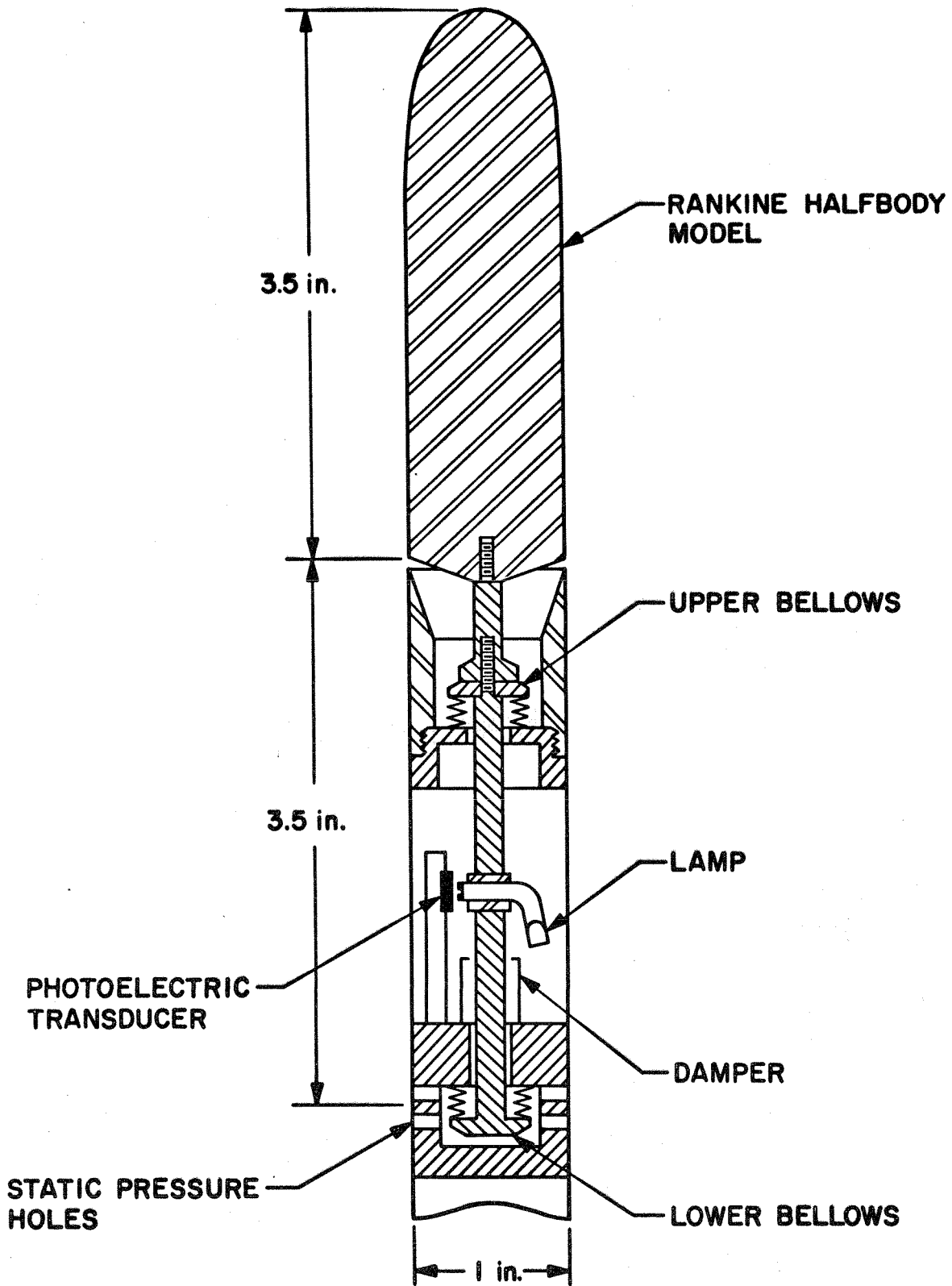


Figure 3. DESIGN OF DRAG BALANCE

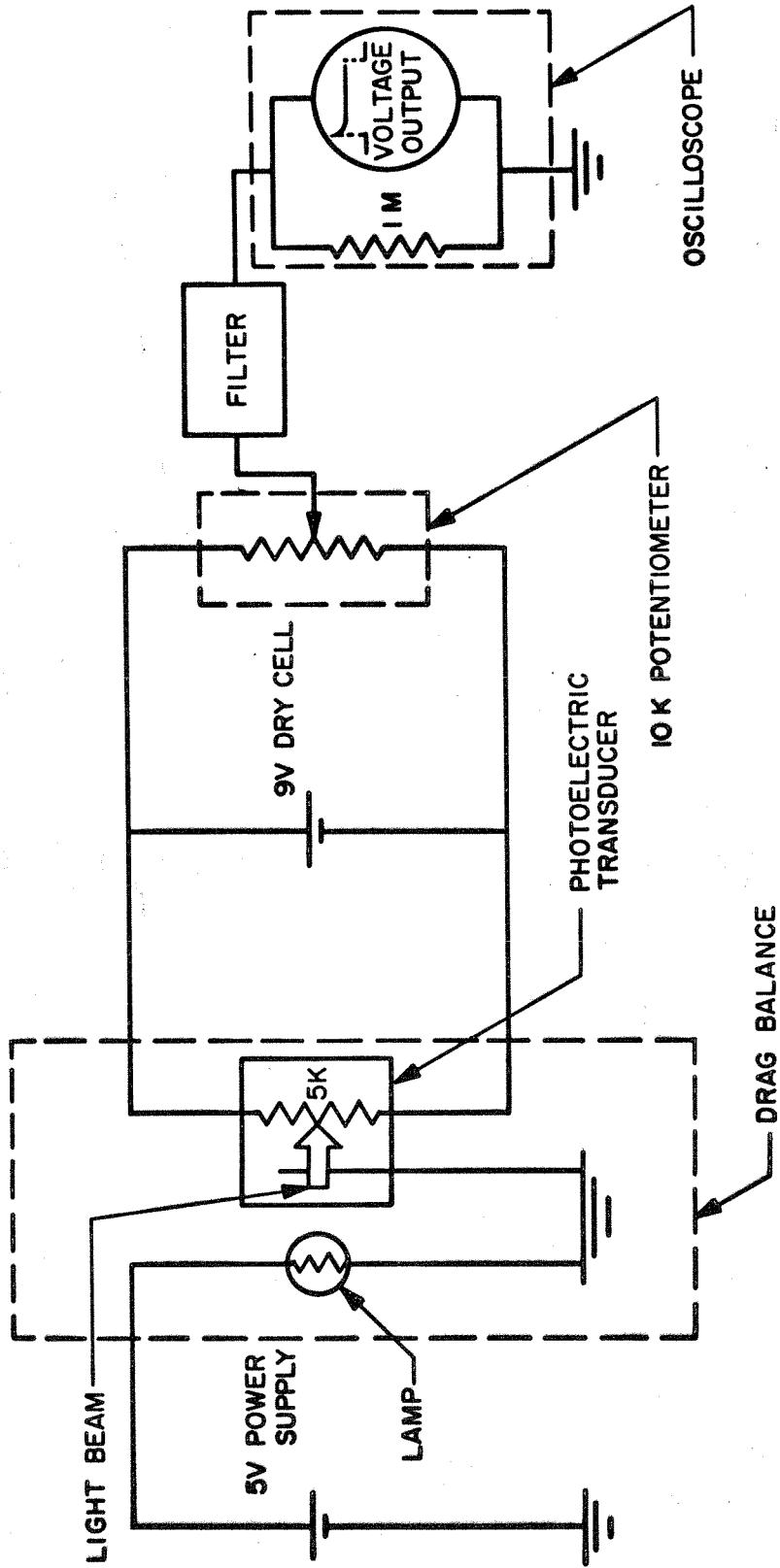
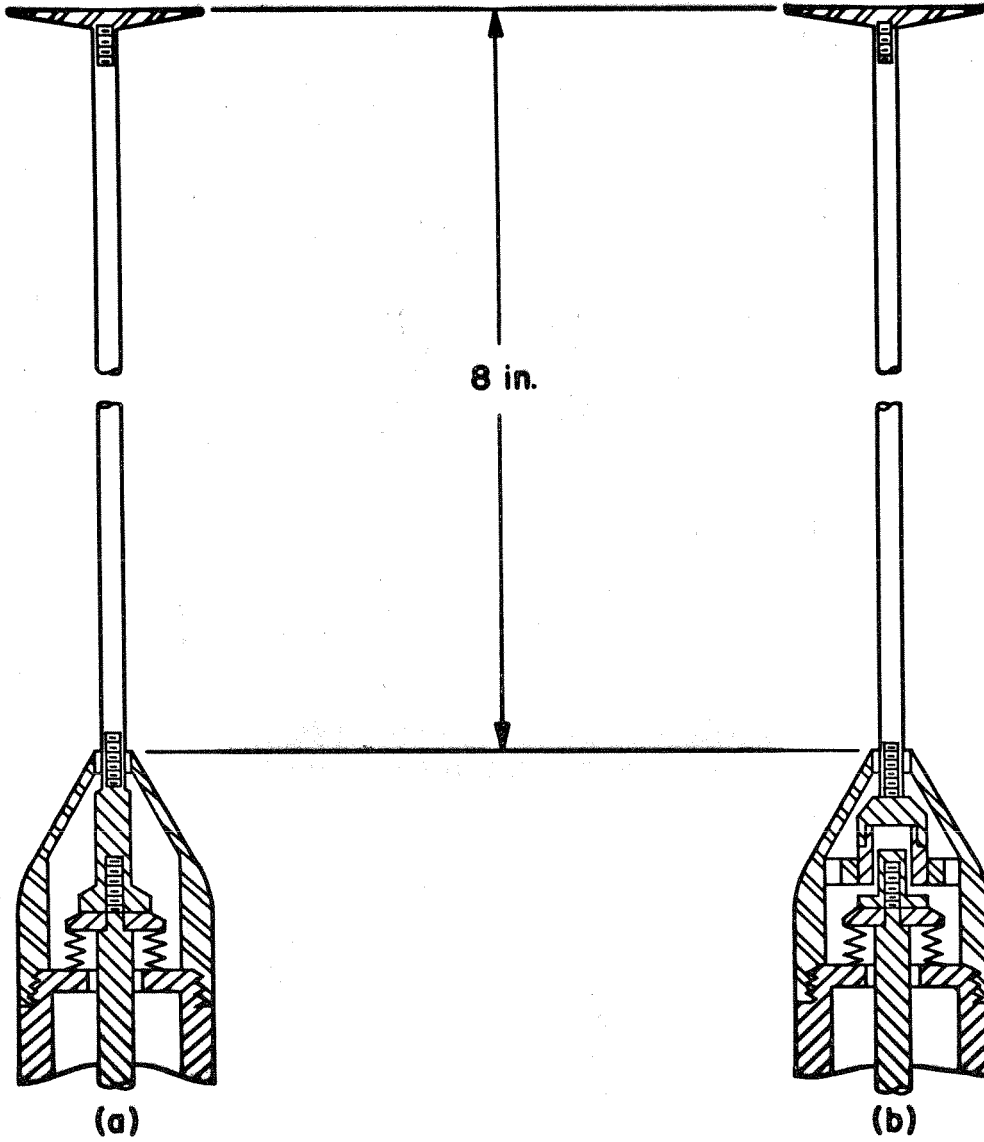


Figure 4. DIAGRAM OF THE DRAG BALANCE ELECTRICAL CIRCUIT



**Figure 5. DRAG BALANCE SET-UPS FOR FLAT DISK:
(a) TOTAL DRAG SET-UP, (b) TARE DRAG SET-UP**

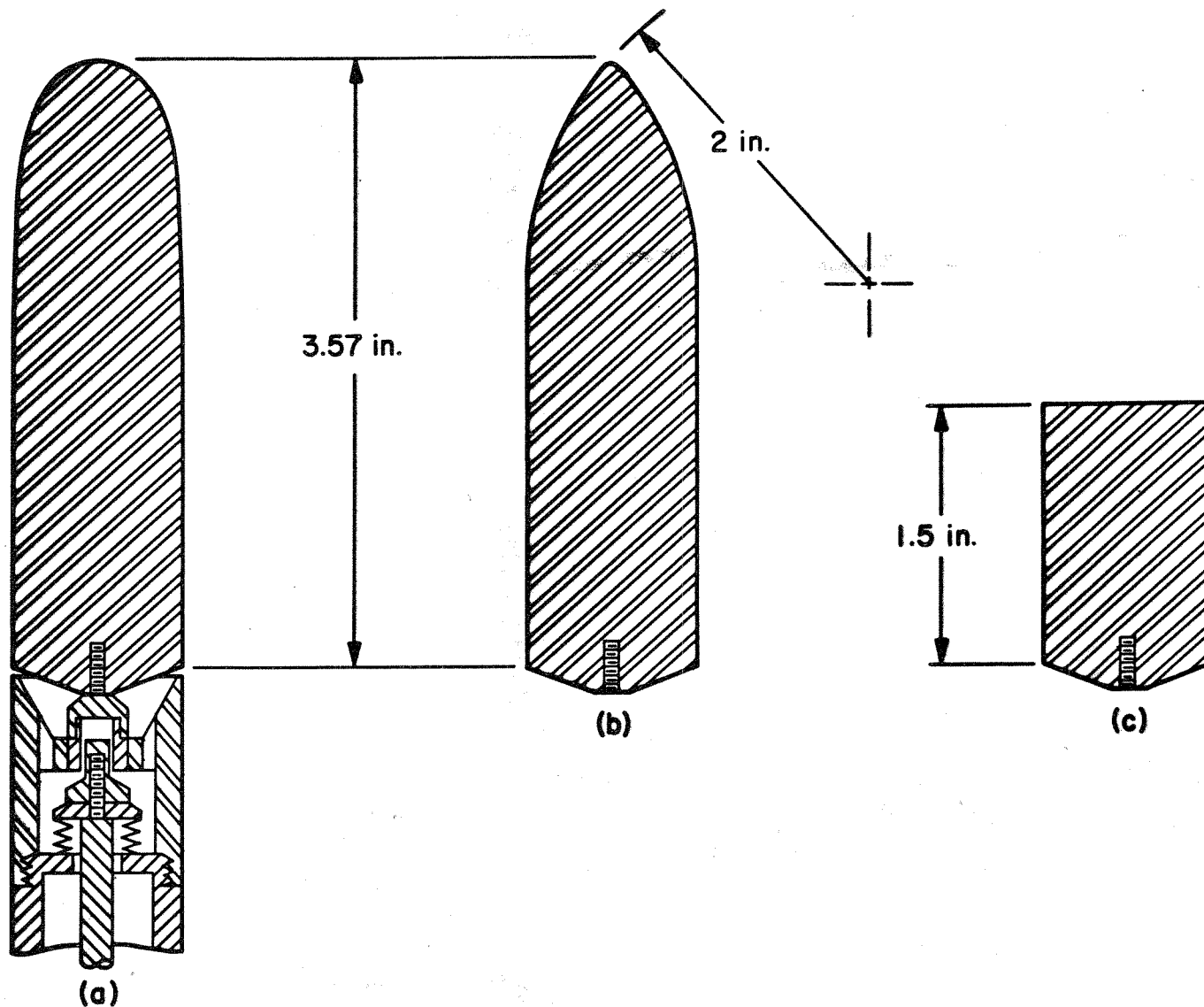


Figure 6. HEAD FORMS OF SEMI-INFINITE BODIES: (a) RANKINE HALFBODY WITH TARE DRAG SET-UP, (b) OGIVE HALFBODY, (c) BLUNT HALFBODY

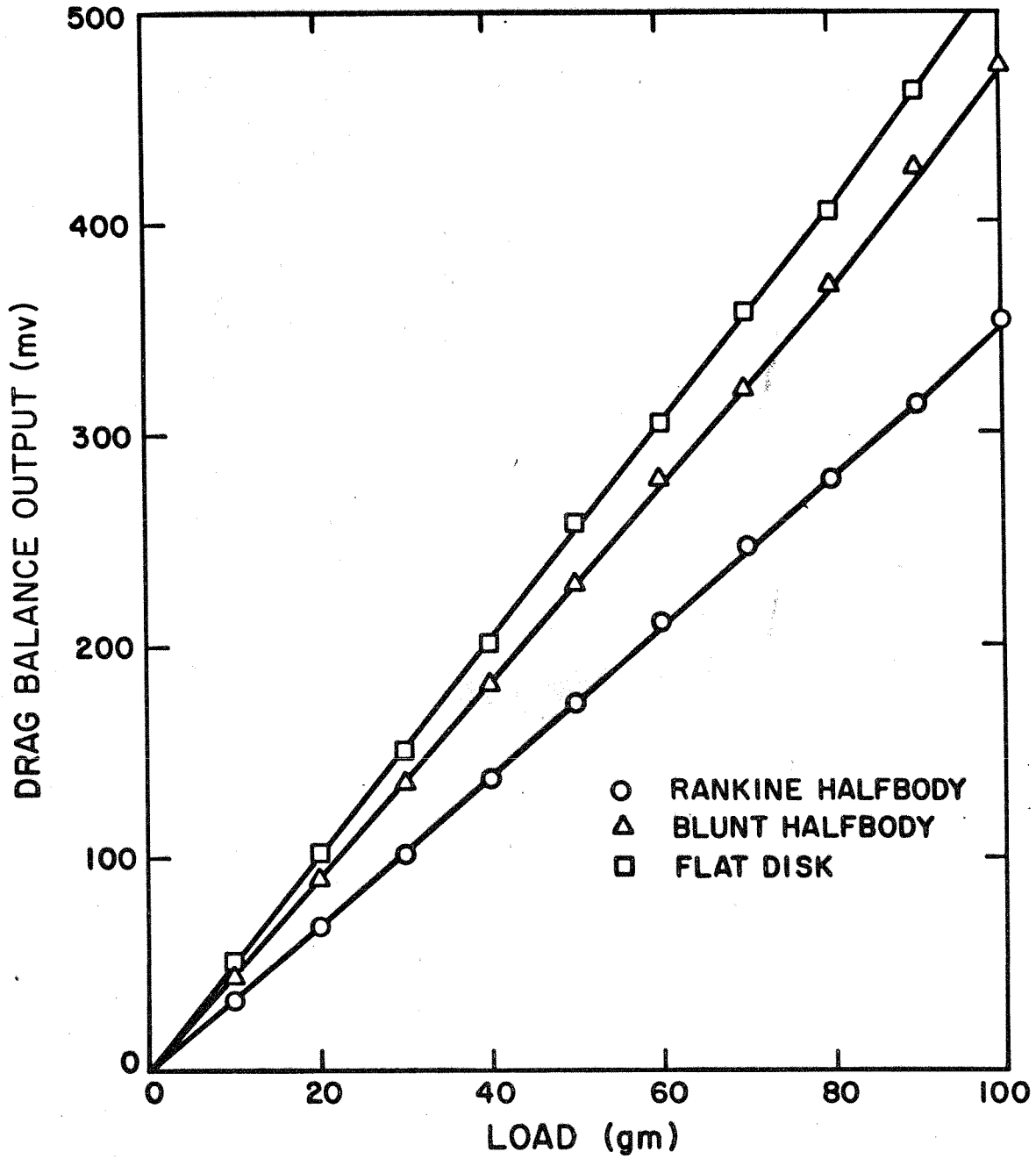
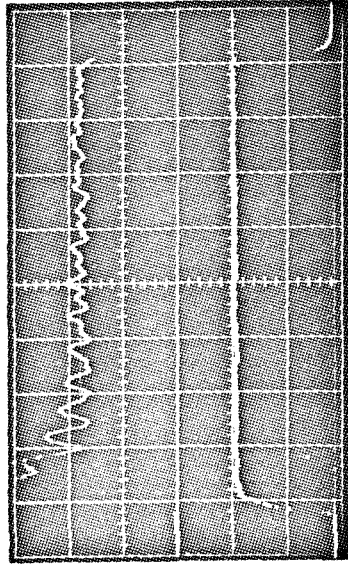
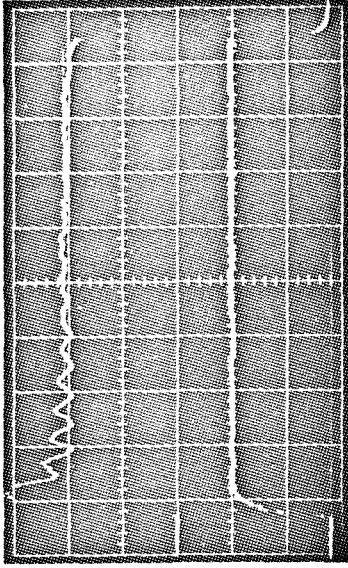


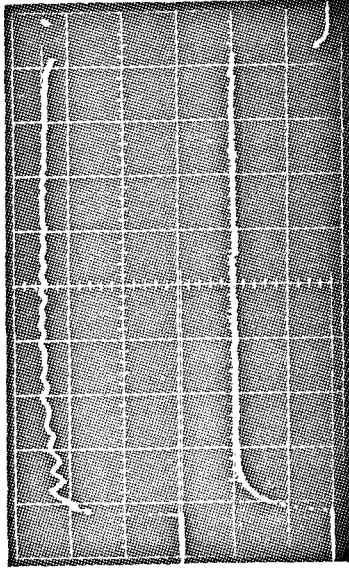
Figure 7. TYPICAL DRAG BALANCE CALIBRATION CURVES



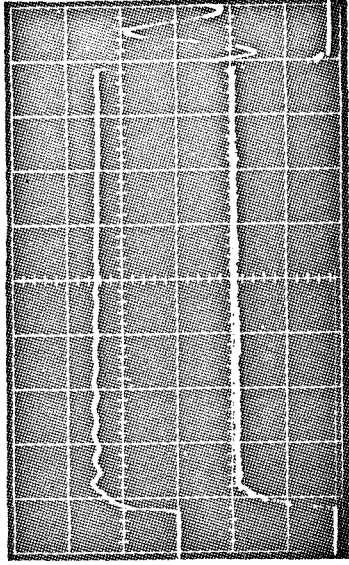
(a) $B_0 = 0$, $D = 2.5$ gm
Upper Trace: 5 mv/div



(b) $B_0 = 3,300$ g, $D = 7.0$ gm
Upper Trace: 10 mv/div



(c) $B_0 = 6,600$ g, $D = 14.2$ gm
Upper Trace: 20 mv/div

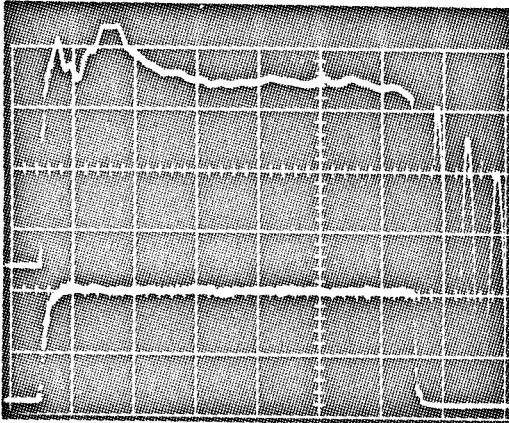


(d) $B_0 = 11,000$ g, $D = 19.6$ gm
Upper Trace: 50 mv/div

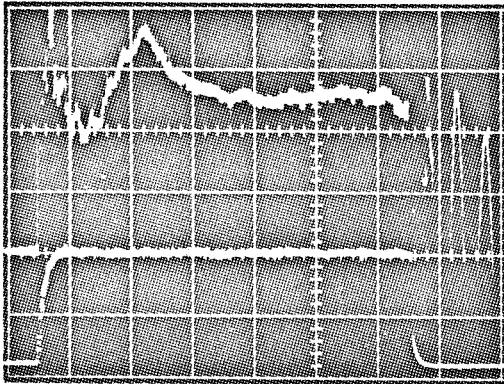
All Lower Traces: .2 v/div

All Sweep Speeds: .3 sec/div

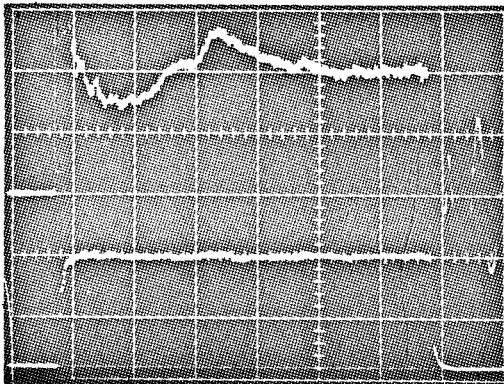
FIGURE 8. DRAG DATA OF RANKINE HALFBODY AT VARIOUS FIELD STRENGTHS AND AT A
FIXED VELOCITY OF 0.3 M/SEC



(a) .50 in. Diameter Disk
Upper Trace: 20 mv/div



(b) .75 in. Diameter Disk
Upper Trace: 50 mv/div



(c) 1.00 in. Diameter Disk
Upper Trace: 100 mv/div

All Lower Traces: .2 v/div

All Sweep Speeds: .5 sec/div

FIGURE 9. TRANSIENT DRAG DATA OF FLAT DISKS AT FIXED VELOCITY OF 0.3 M/SEC

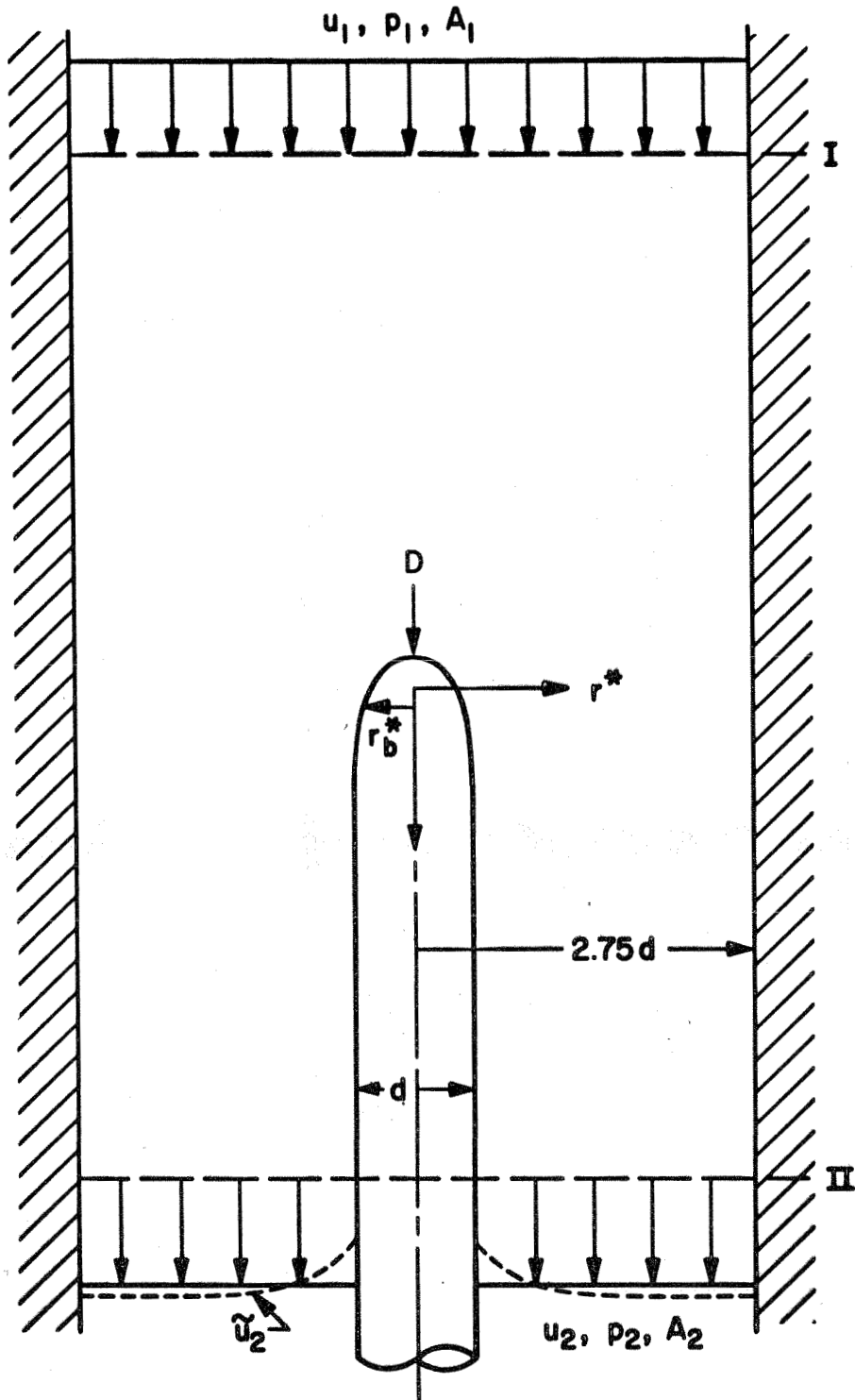


Figure 10. CONTROL VOLUME FOR CALCULATION OF BASE DRAG

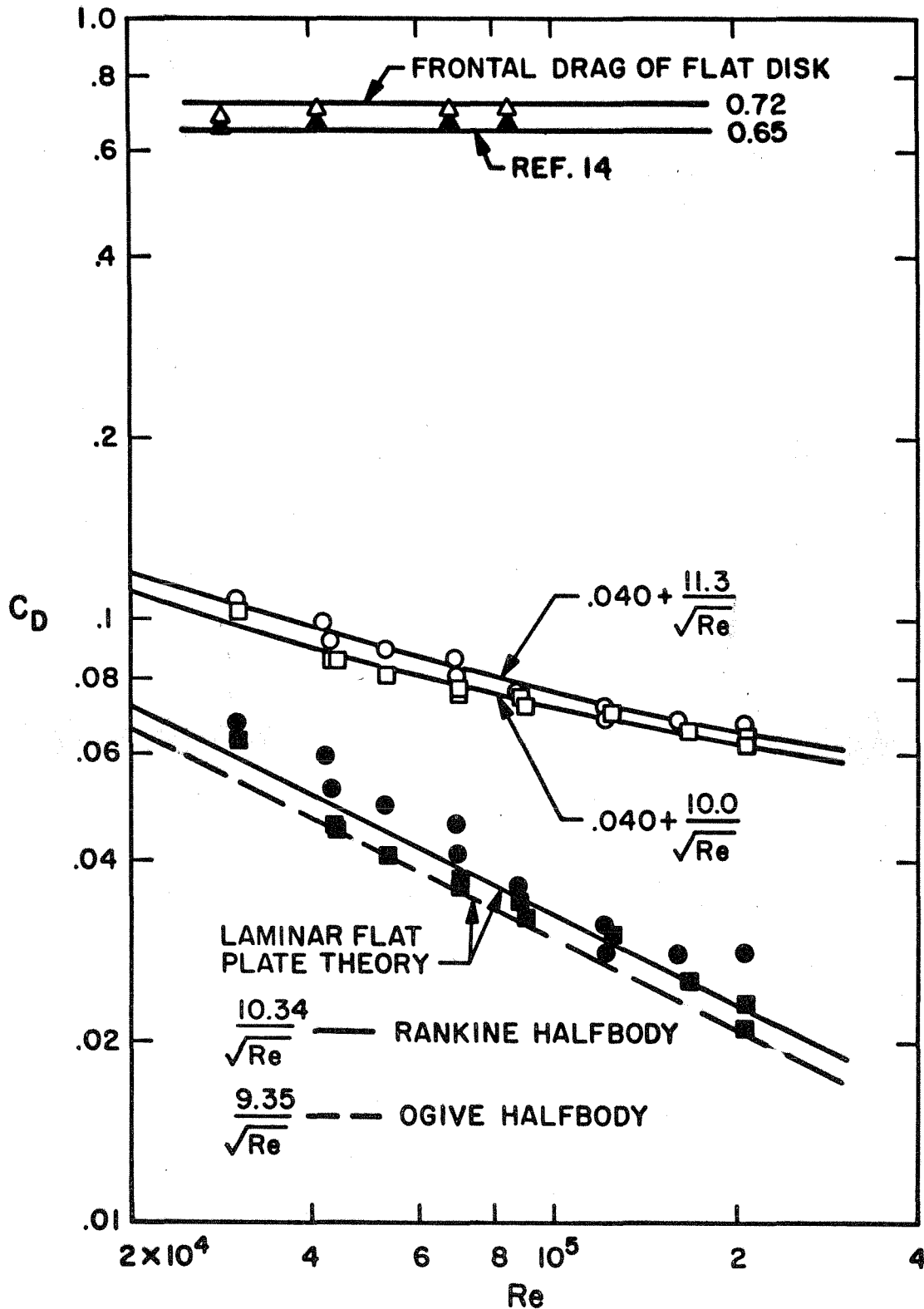


Figure 11. ZERO-FIELD DRAG COEFFICIENTS OF SEMI-INFINITE BODIES VS. REYNOLDS NUMBER

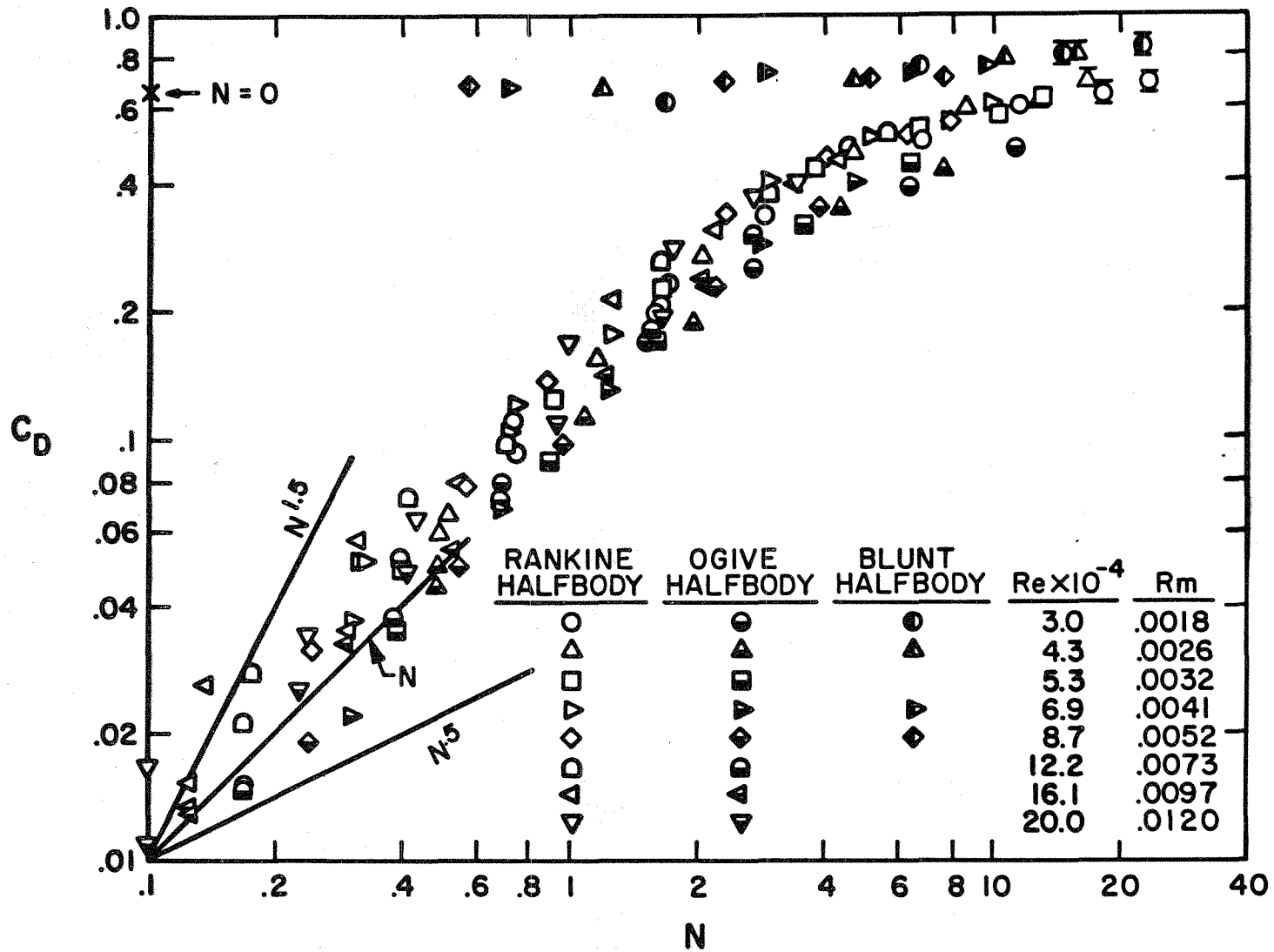


Figure 12 DRAG COEFFICIENTS OF SEMI-INFINITE BODIES VS. INTERACTION PARAMETER

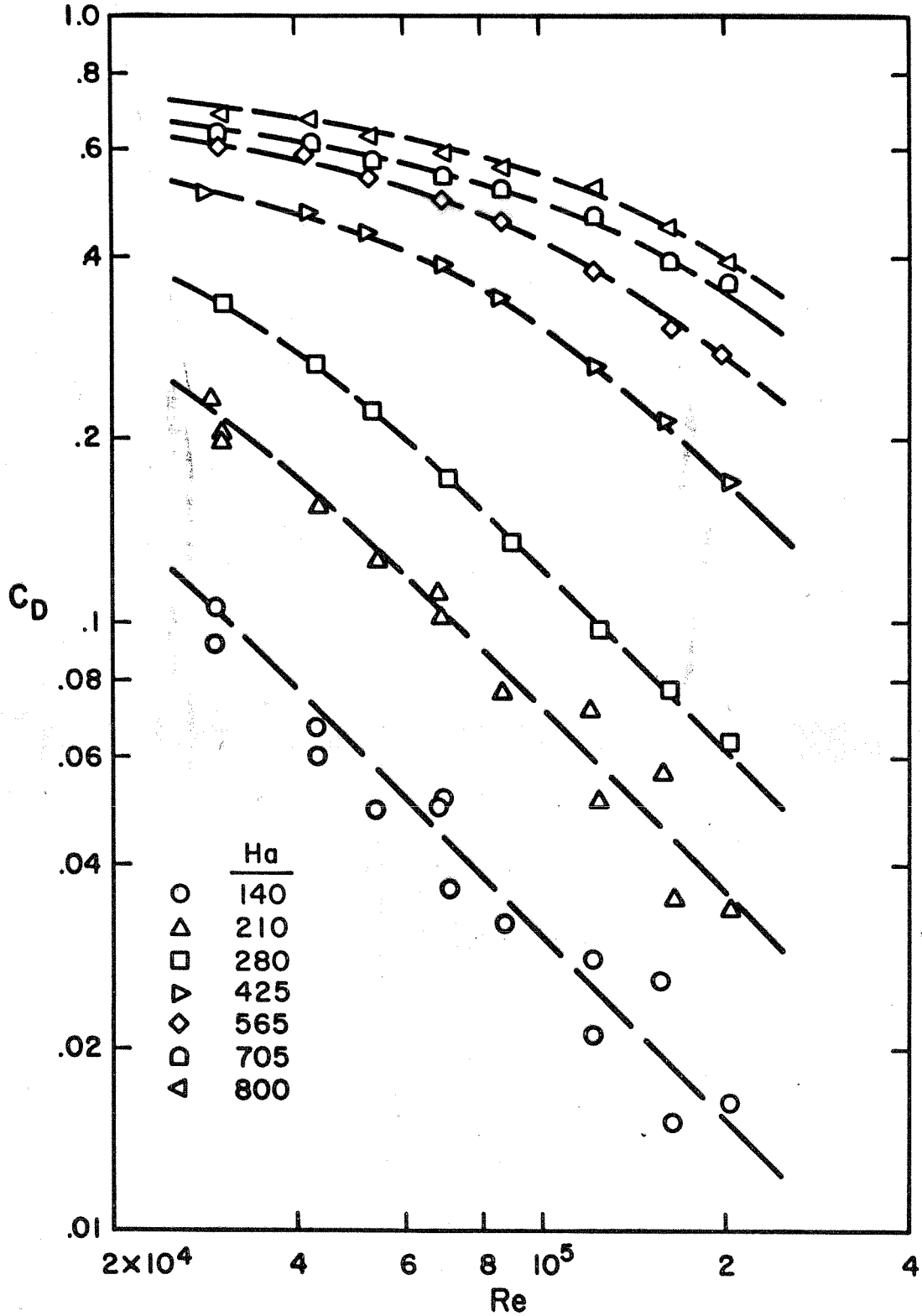


Figure 13. MFD DRAG COEFFICIENT OF RANKINE HALFBODY VS. REYNOLDS NUMBER AT VARIOUS HARTMANN NUMBERS

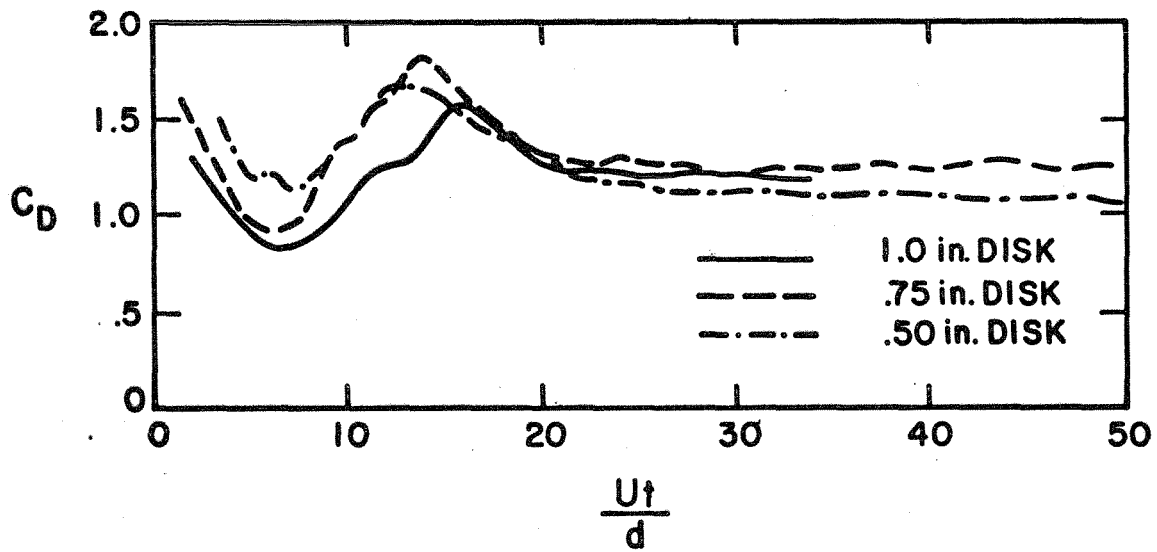
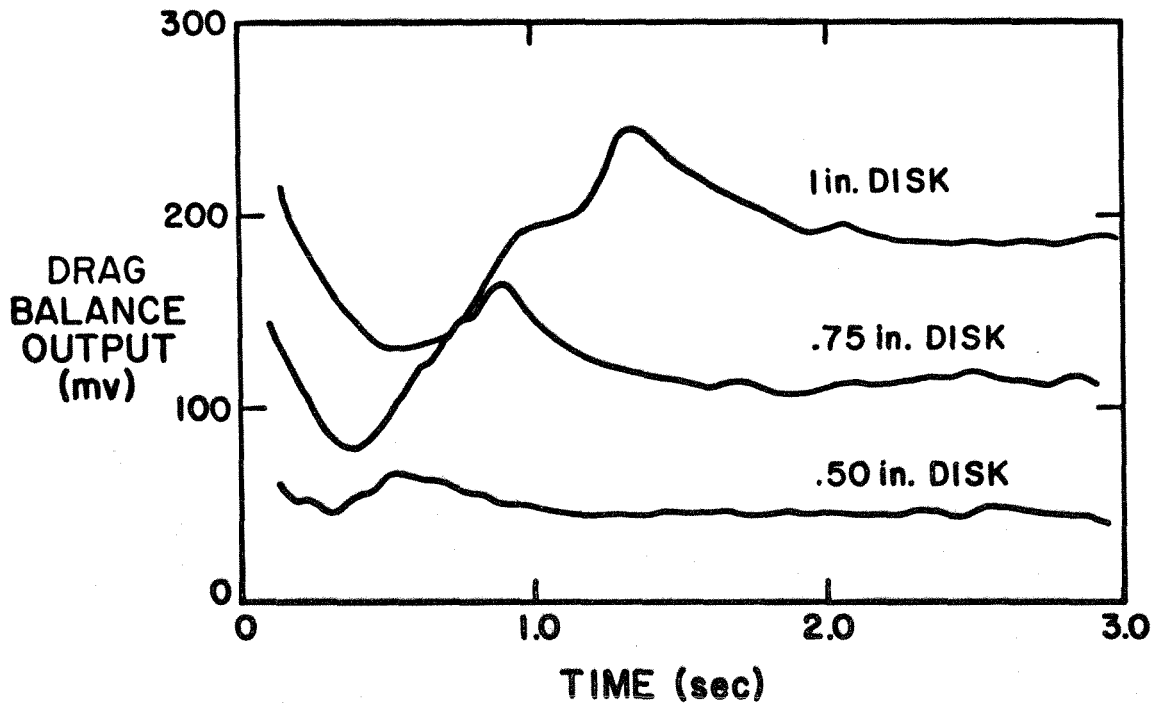


Figure 14. DRAG OF FLAT DISKS STARTED IMPULSIVELY FROM REST TO A CONSTANT VELOCITY OF 0.3 m/sec

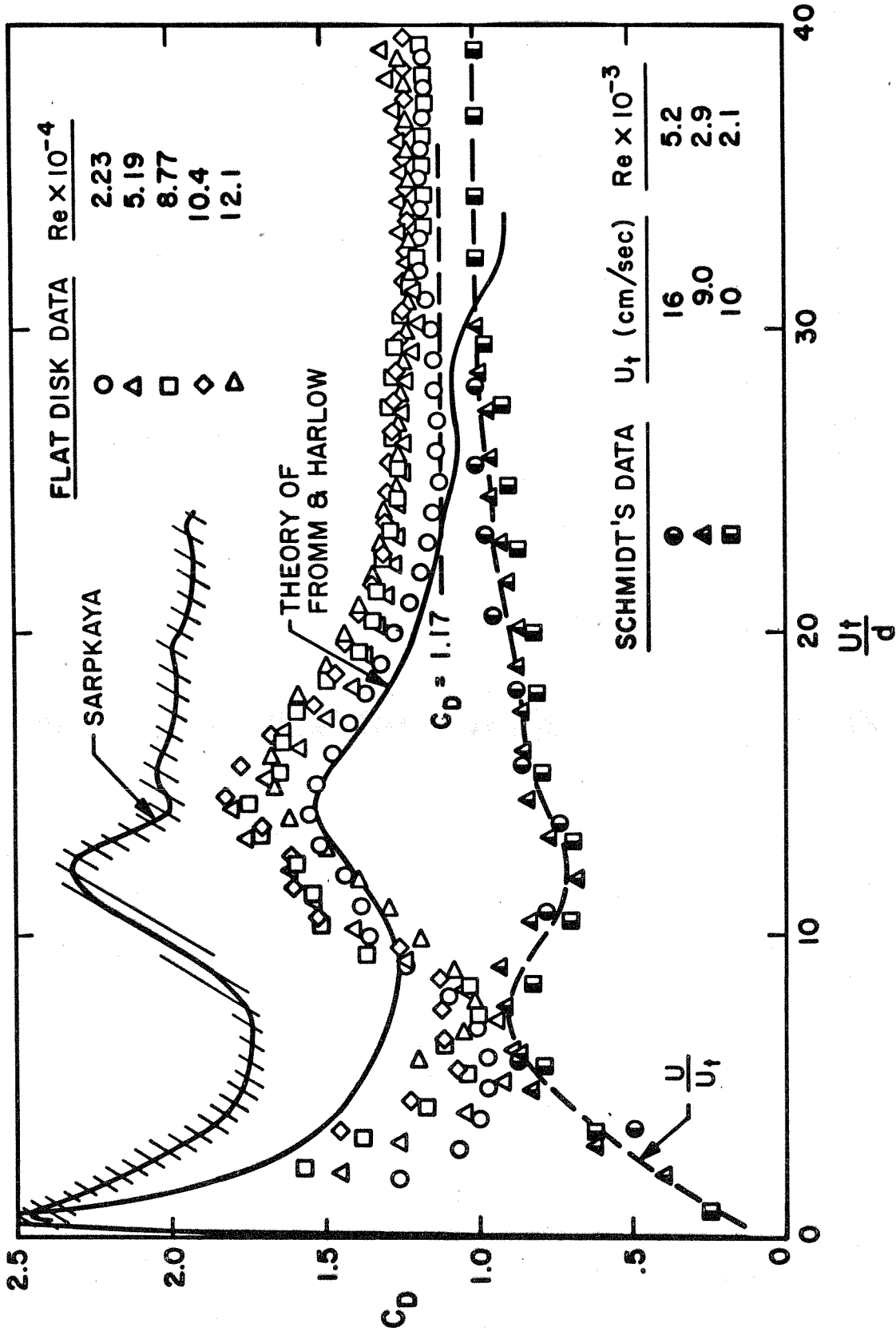


Figure 15. DRAG COEFFICIENT OF 0.75 in. DIAMETER FLAT DISK STARTED IMPULSIVELY FROM REST

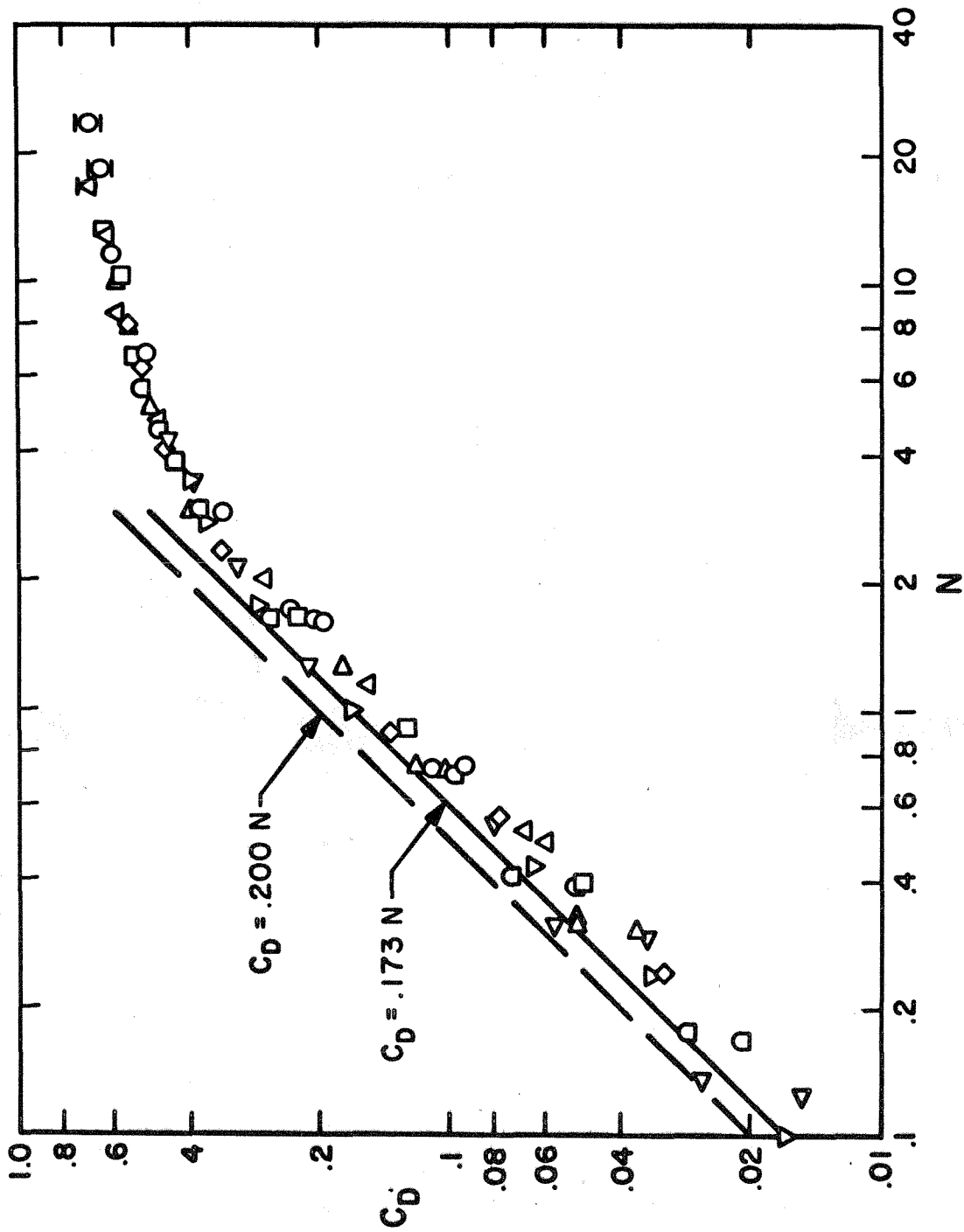


Figure 16. MFD DRAG COEFFICIENT OF RANKINE HALFBODY VS. INTERACTION PARAMETER

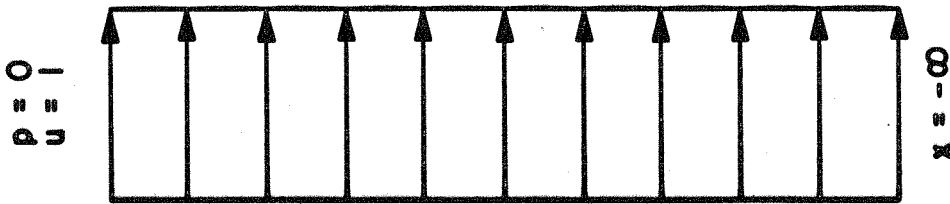
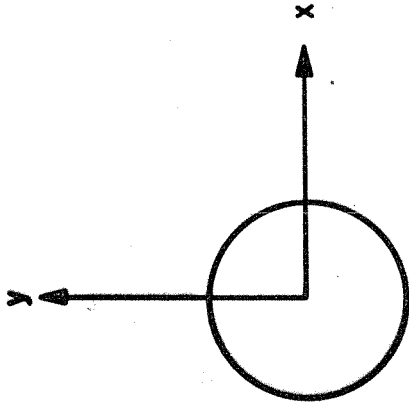
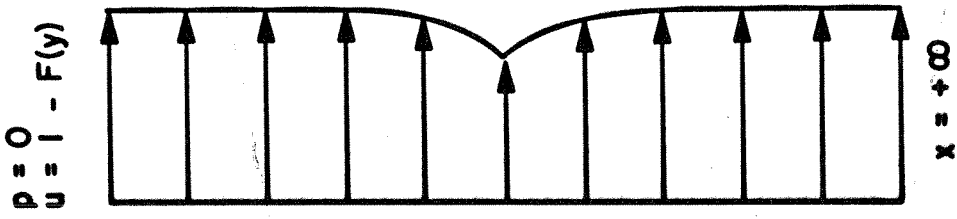
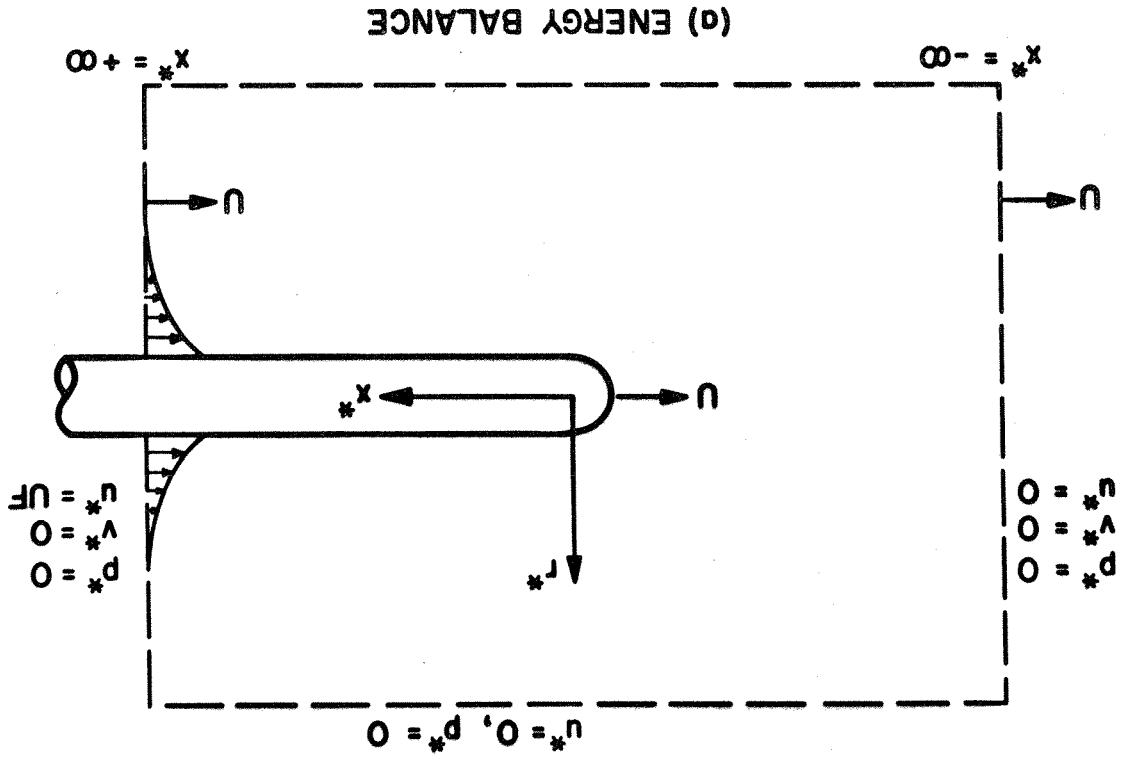
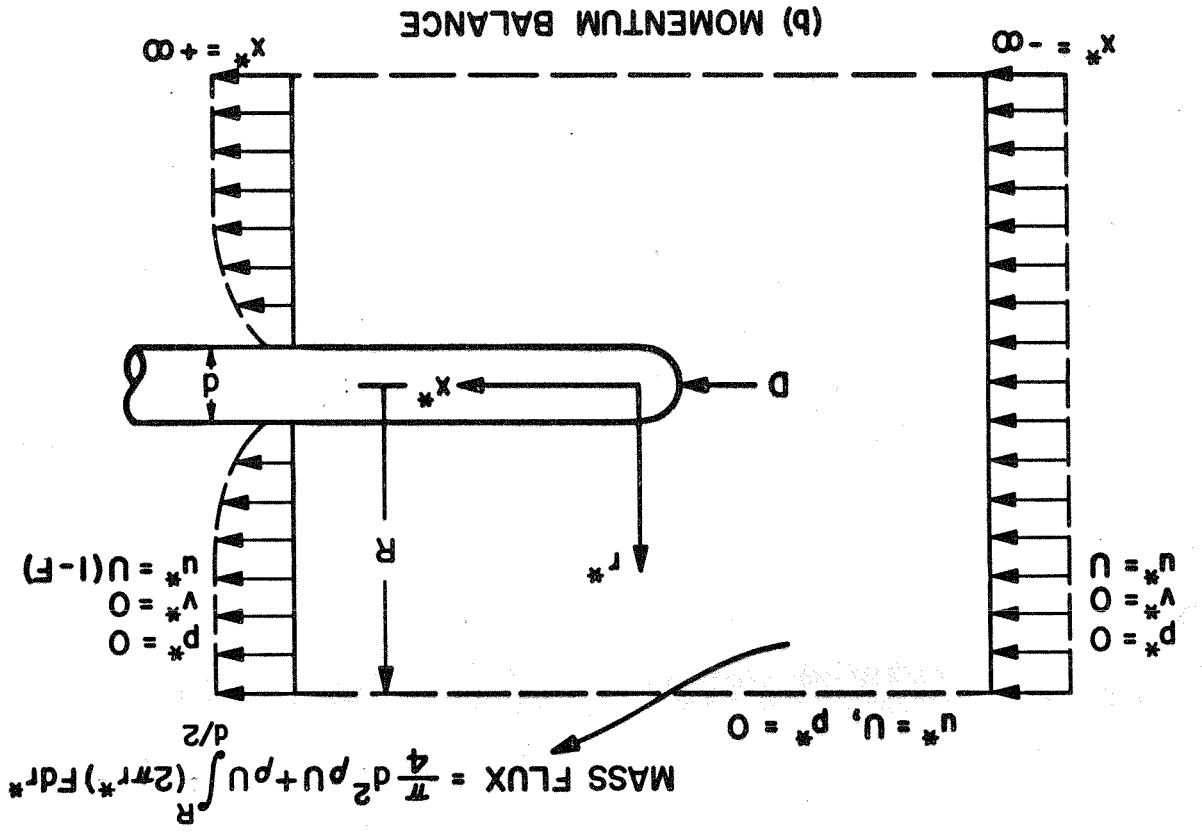


Figure 17. TAMADA'S SOLUTION (REF. 32) FOR INVISCID MFD FLOW PAST A TWO-DIMENSIONAL CIRCULAR CYLINDER AT $N = .4$

Figure 18. CONTROL VOLUMES FOR CALCULATION OF MFD DRAG



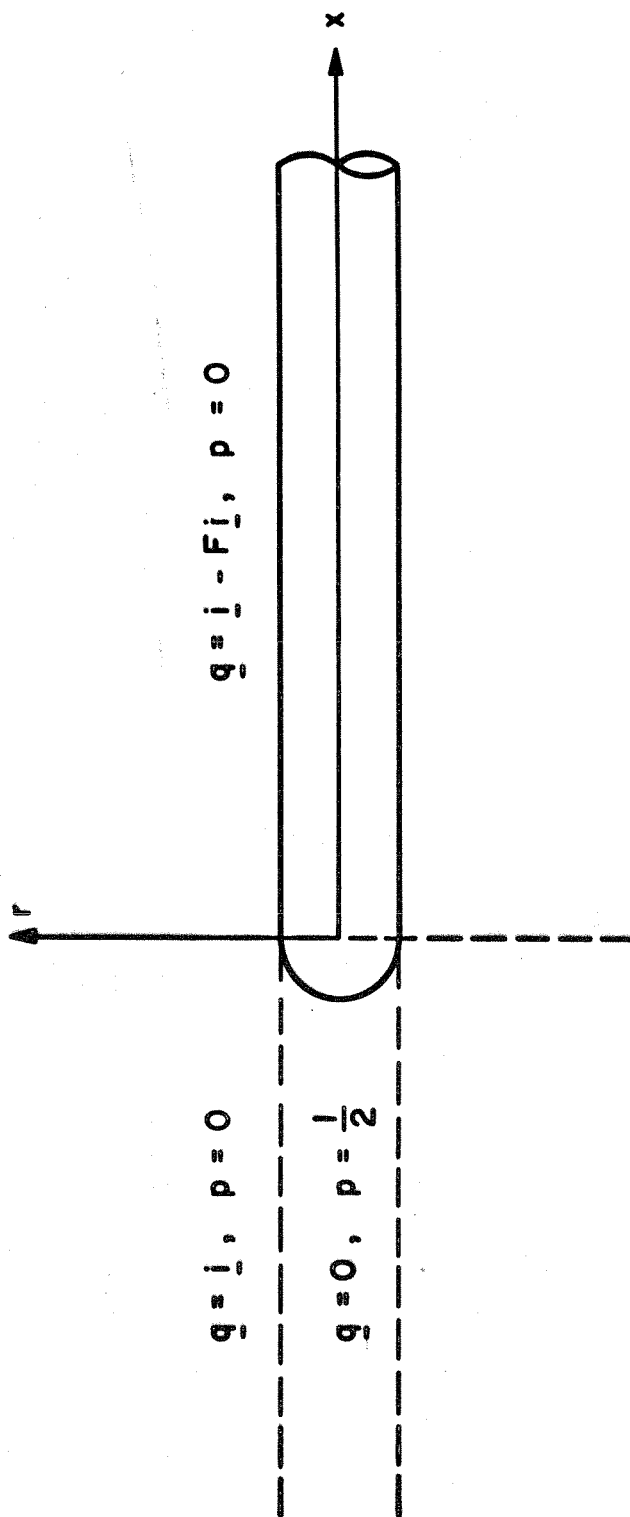


Figure 19. SOLUTION FOR THE LIMIT $N \rightarrow \infty$

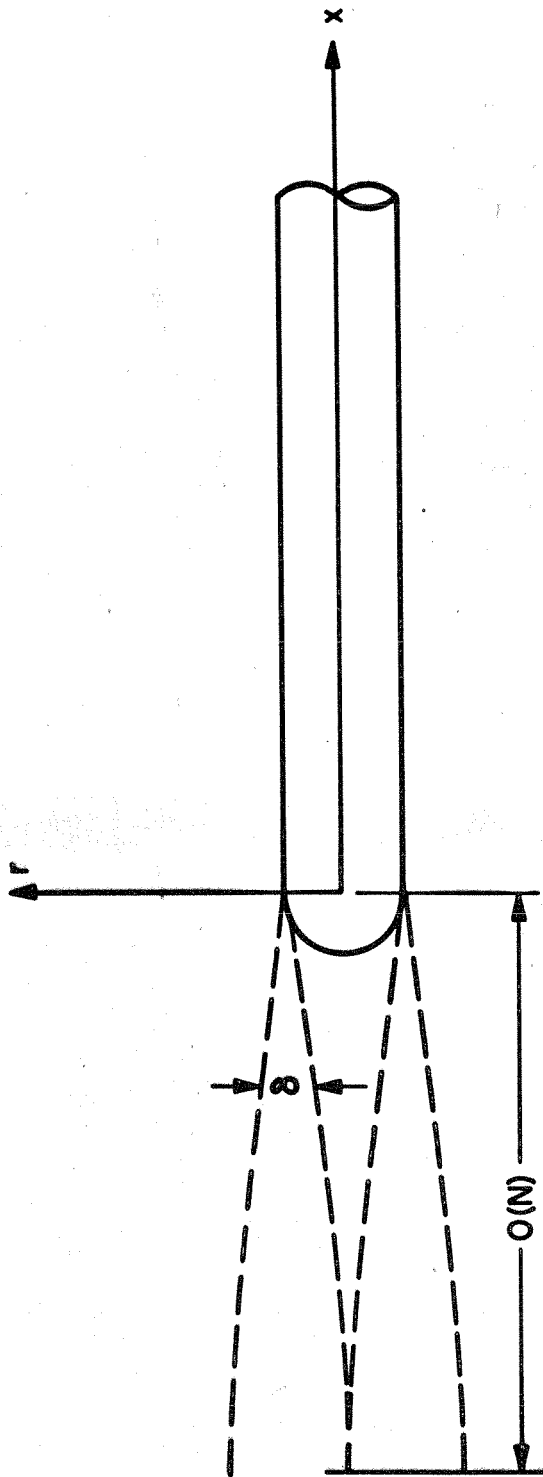


Figure 20. DEVELOPMENT OF CURRENT LAYERS FOR $N \gg 1$

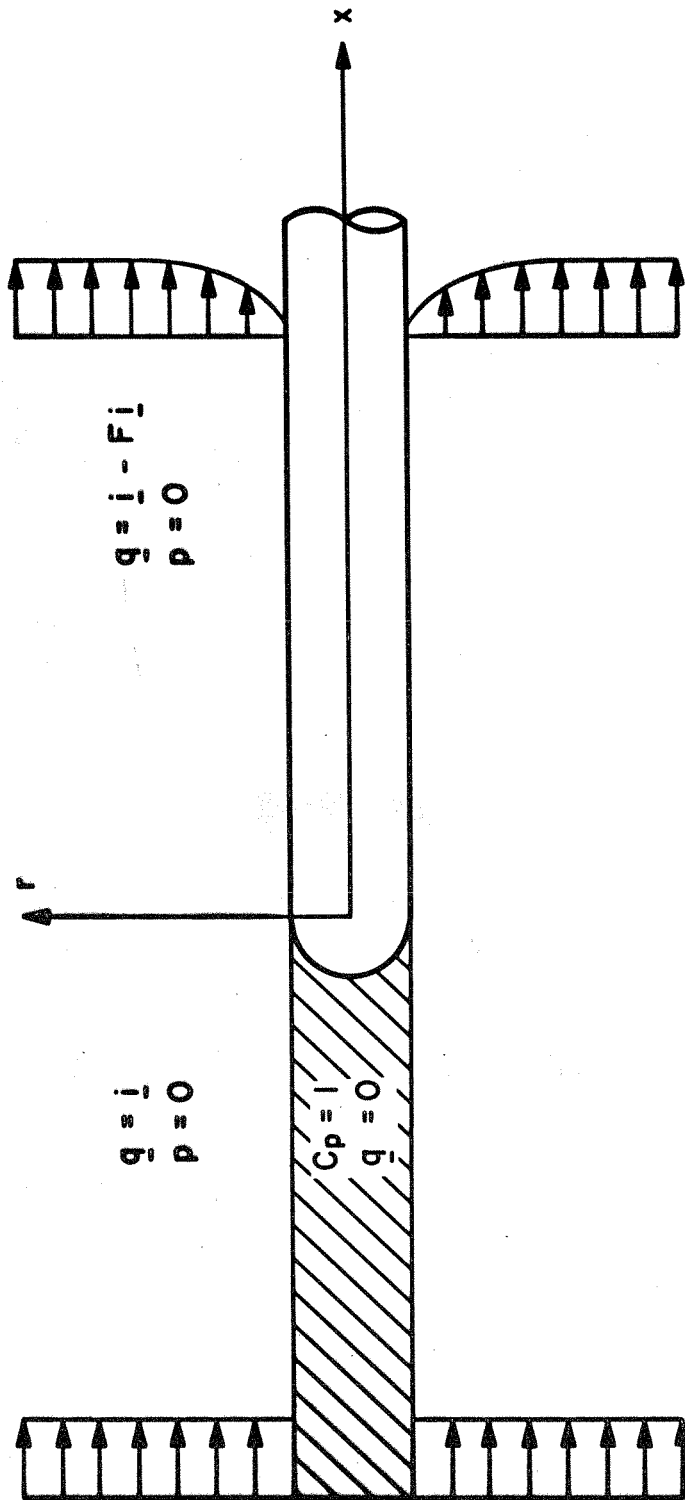


Figure 21. ULTIMATE FLOW FIELD IN THE LIMIT AS $N \rightarrow \infty$